

---

Doctoral Dissertations

Student Theses and Dissertations

---

2012

## An Improved dipole-moment model based on near-field scanning for characterizing near-field coupling and far-field radiation from an IC

Zhenwei Yu

Follow this and additional works at: [https://scholarsmine.mst.edu/doctoral\\_dissertations](https://scholarsmine.mst.edu/doctoral_dissertations)



Part of the [Electrical and Computer Engineering Commons](#)

Department: **Electrical and Computer Engineering**

---

### Recommended Citation

Yu, Zhenwei, "An Improved dipole-moment model based on near-field scanning for characterizing near-field coupling and far-field radiation from an IC" (2012). *Doctoral Dissertations*. 2072.  
[https://scholarsmine.mst.edu/doctoral\\_dissertations/2072](https://scholarsmine.mst.edu/doctoral_dissertations/2072)

This thesis is brought to you by Scholars' Mine, a service of the Missouri S&T Library and Learning Resources. This work is protected by U. S. Copyright Law. Unauthorized use including reproduction for redistribution requires the permission of the copyright holder. For more information, please contact [scholarsmine@mst.edu](mailto:scholarsmine@mst.edu).

AN IMPROVED DIPOLE-MOMENT MODEL BASED ON NEAR-FIELD  
SCANNING FOR CHARACTERIZING NEAR-FIELD COUPLING AND FAR-FIELD  
RADIATION FROM AN IC

by

ZHENWEI YU

A DISSERTATION

Presented to the Faculty of the Graduate School of the  
MISSOURI UNIVERSITY OF SCIENCE AND TECHNOLOGY

In Partial Fulfillment of the Requirements for the Degree

DOCTOR OF PHILOSOPHY

in

ELECTRICAL ENGINEERING

2012

Approved  
Jun Fan, Advisor  
James Drewniak  
Richard DuBroff  
David Pommerenke  
Daryl Beetner  
Barbara Hale

## **PUBLICATION DISSERTATION OPTION**

This dissertation has been prepared in the form of four papers for publication.

The first paper consisting of pages 3 to 32 is AN IMPROVED DIPOLE-MOMENT MODEL BASED ON NEAR-FIELD SCANNING FOR CHARACTERIZING NEAR-FIELD COUPLING AND FAR-FIELD RADIATION FROM AN IC. This extended work has been submitted to IEEE Transaction on Electromagnetic Compatibility. The second paper consisting of pages from 33 to 48 is focused on the HEAT-SINK MODELING AND DESIGN WITH DIPOLE MOMENTS REPRESENTING IC EXCITATION, and has been submitted to IEEE Transaction on Electromagnetic Compatibility. The third paper consisting of pages from 49 to 70 is AN EFFECTIVE DIELECTRIC PROPERTY OF LAYERED MEDIA FOR CAVITY MODEL APPLICATIONS, and is to be submitted to IEEE Transaction on Electromagnetic Compatibility. The fourth paper consisting of pages from 71 to 80 is MULTIMODE S-PARAMETER CHARACTERIZATION FOR MULTI-PORT PASSIVE STRUCTURES, and is to be submitted to IEEE Transaction on Electromagnetic Compatibility.

## ABSTRACT

Radio Frequency Interference (RFI) problems are critical issues in wireless platform design. The accurate noise model of integrated circuits (ICs) is needed to help designers to diagnose and predict RFI problems. In this dissertation, an improved IC radiated emission model based on near-field measurements is proposed. The regularization technique and the truncated SVD method are employed together with the least square method to calculate the dipole moments from the near-field data. This dipole model has clear physical meaning: the electric and magnetic dipoles represent the voltage and the current in the circuit, respectively.

One application of this dipole model is the prediction of heat sink radiation. In order to accurately predict the fields excited by a heat sink, an approach is proposed in this paper to include the exact excitation of the heat sink, which is described by some dipole moments constructed from the near-field scanning of the integrated circuit beneath the heat sink.

Another contribution of the work is the proposal of effective dielectric properties of layered media for cavity model applications. With the effective properties, the cavity model can be generalized for either parallel plates or metal enclosures containing multiple dielectric layers.

In the fourth paper a unified s-parameter (multimode s-parameter) representation for a multiport passive structure is proposed. Both mixed-mode and single-ended s-parameters are included in the unified representation, which makes it more convenient to characterize structures.

## ACKNOWLEDGMENTS

I would like to thank my advisor, Dr. Jun Fan for his advice, guidance, and patience. Special thanks to my committee members, Dr. James Drewniak, Dr. Richard DuBroff, Dr. David Pommerenke, Dr. Daryl Beetner and Dr. Barbara Hale for their time and effort in reviewing this dissertation. Thanks to Kevin, Jason, and Soji with Physical Technology Lab of Intel for their guidance and useful discussions.

My heartfelt gratitude goes to my parents for their support and encouragement towards achieving this goal.

## TABLE OF CONTENTS

	Page
PUBLICATION DISSERTATION OPTION.....	iii
ABSTRACT.....	iv
ACKNOWLEDGMENTS.....	v
LIST OF ILLUSTRATIONS.....	ix
LIST OF TABLES.....	xii
 SECTION	
1. INTRODUCTION.....	1
 PAPER	
I. AN IMPROVED DIPOLE-MOMENT MODEL BASED ON NEAR-FIELD SCANNING FOR CHARACTERIZING NEAR-FIELD COUPLING AND FAR- FIELD RADIATION FROM AN IC.....	3
Abstract.....	3
I. INTRODUCTION.....	3
II. ELECTROMAGNETIC FIELDS OF DIPOLE MOMENTS.....	6
III. DIPOLE MODEL EXTRACTION.....	11
A. Regularization Technique.....	14
B. Truncated Singular-Value Decomposition (SVD) Method.....	16
C. Relationship between Regularization and Truncated SVD Approaches .....	18
IV. VALIDATION AND DISCUSSIONS.....	19
V. EXPERIMENTAL VALIDATION.....	25
VI. CONCLUSIONS.....	28
VII. REFERENCE.....	28

II. HEAT-SINK MODELING AND DESIGN WITH DIPOLE MOMENTS REPRESENTING IC EXCITATION.....	33
Abstract.....	33
I. INTRODUCTION.....	33
II. AN IMPROVED DIPOLE-MOMENT MODEL OF IC.....	35
III. INCORPORATION OF IMPROVED DIPOLE-MOMENT MODEL IN HEAT-SINK MODELING.....	37
IV. CONCLUSIONS.....	45
V. REFERENCE.....	45
III. AN EFFECTIVE DIELECTRIC PROPERTY OF LAYERED MEDIA FOR CAVITY MODEL APPLICATIONS.....	49
Abstract.....	49
I.INTRODUCTION.....	49
II. CAVITY MODEL.....	51
III. THE EFFECTIVE DIELECTRIC PROPERTY OF THE CAVITY MODEL.....	55
A. Two-layer media.....	55
B. Multilayered media.....	62
C. Validations.....	65
IV.CONCLUSION.....	68
V. REFERENCE.....	69
IV. MULTIMODE S-PARAMETER CHARACTERIZATION FOR MULTIPOINT PASSIVE STRUCTURES.....	71
Abstract .....	71
I. INTRODUCTION.....	71
II. EXAMPLES.....	75

III. CONCLUSIONS.....79

IV. REFERENCES.....79

SECTION

2. CONCLUSIONS.....81

VITA.....84



## LIST OF ILLUSTRATIONS

Figure	Page
<b>PAPER I</b>	
1 Equivalent source model using a dipole array .....	11
2 Geometry of an example.....	14
3 Equivalent sources calculated using the conventional least square method.....	14
4 Improved dipole-moment model extracted using the regularization technique.....	16
5 Improved dipole moment model extracted using the truncated SVD approach.....	18
6 Validation: near-field scanning plane, 100-mil-high validation plane, and 3 meter far-field observation points.....	19
7 Validation of the improved dipole-moment sources.....	19
8 Comparisons of the field magnitudes along the $y=0$ axis at the plane 30 mils above the ground plane from the original structure.....	21
9 Charge on the trace and the ground plane due to a potential difference.....	23
10 Calculation of an electric dipole moment.....	23
11 Calculation of a magnetic dipole moment.....	23
12 Dipole moments extracted using the regularization technique for the test geometry shown in Fig. 2 at 100 MHz.....	24
13 The DUT and the scanned fields.....	26
14 Field dipoles and field generated by the dipoles.....	27
<b>PAPER II</b>	
1 Equivalent dipole-moment model for field calculations from an IC, based on near-field scanning measurements.....	36
2 Generating a realistic excitation for heat-sink studies using dipole moments to replace the IC underneath the heat sink.....	38
3 The text file used in EMC Studio to describe the information of a dipole.....	39

4	A x-directional magnetic dipole: different magnetic dipole definitions.....	39
5	An example trace structure used to mimic an IC.....	40
6	The equivalent dipole moments for the trace structure shown in Fig.5, obtained using the regularization approach from near-field data.....	40
7	The heat-sink structure simulated.....	42
8	Comparisons between the calculated fields from the heat-sink models in Fig. 7.....	42
9	Comparisons between the calculated Ez component at 3 meters away from the heat-sink models shown in Fig. 7.....	43
10	Another heat-sink structure simulated.....	44
11	Comparisons between the calculated fields from the heat-sink models in Fig. 10.....	45
PAPER III		
1	Structures with dielectric layers.....	50
2	A parallel plane pair excited by impressed current.....	52
3	A structure with a layered medium.....	56
4	The input impedance seen looking up at the interface.....	57
5	Effective dielectric property $\epsilon_{eff}$ for layered media.....	60
6	The effective dielectric property $\epsilon_{eff}$ for a three-layer medium.....	62
7	A PCB with three-layer media.....	66
8	The transfer impedance calculated using the effective dielectric property and the result from a full-wave simulation tool.....	66
9	A metallic enclosure with three layers of dielectric.....	67
10	The effective dielectric property of a metallic enclosure.....	67
11	The transfer impedance calculated using the effective dielectric property and the result by a full-wave simulation tool.....	68

PAPER IV

1 A 4-layer printed circuit board with multiple vias.....76

2 A set of dipole and monopole antennas.....78

**LIST OF TABLES**

Table	Page
PAPER I	
I Comparisons of dipole moments.....	25
PAPER IV	
I The port mapping from single-ended port to mixed-mode port.....	74

## 1. INTRODUCTION

People need mobility.

There is an increasing market for wireless devices such as smartphones, laptop computers, and etc. while the dimensions of a wireless platform become smaller, clock frequencies become higher, and more antennas are integrated into the platform. RFI problems become more and more serious. The noise due to the radiated emissions from an IC has significant impact on the performance of radio communication systems. An effective model of RFI problems is desirable to enable tighter platform integration, reduce RFI and EMI compliance cost. This model will be able to help wireless platform producers deliver differentiated products with excellent RFI/EMI performance at lower costs.

General methodologies of RFI modeling include three parts: IC source modeling, antenna modeling, and coupling path modeling. Near-field (NF) scanning technique is widely used to characterize the radiation from a source in the time or frequency domain. Electric and magnetic fields in a scanning plane can be obtained, and IC radiated-emission noise can be extracted based on the field data.

This dissertation consists of four papers. Paper 1 proposes an improved dipole-moment model based on the near-field scanning for characterizing near-field coupling and far-field radiation from an IC. Paper 2 discusses the applications of this model: a methodology for heat-sink modeling and design with dipole moments representing IC excitation. Paper 3 proposes effective dielectric properties of layered media for cavity model applications. With the effective properties, the cavity model can be generalized for

modeling both parallel plates or metal enclosures containing multiple dielectric layers.

Paper 4 proposes a multimode s-parameter representation for multiport passive structures.

The primary contributions of this dissertation include:

An improved dipole-moment model for IC radiated emissions based on the near field scanning data (paper 1).

Physical meaning of the dipole model: an electric dipole represents the voltage and a magnetic dipole represents the current in a trace (paper 1).

The regularization and singular value decomposition (SVD) approaches that are developed to solve the numerical instability issue of the inverse problem to obtain the dipole source (paper 1).

Validations of the model by simulations and measurements (paper 1).

An approach to include the exact excitation of a heat sink, which is described by some dipole-moments constructed from the near-field scanning of the integrated circuit beneath the heat sink. This approach can accurately predict the fields excited by a heat sink. This is essentially an application of the dipole-moment model (paper 2).

Effective dielectric properties of layered media, which generalize the cavity model for parallel plates or metal enclosures containing multiple dielectric layers (paper 3).

A unified s-parameter (multimode s-parameter) representation for multiport passive structures. Both mixed-mode and single-ended s-parameters are included in the unified representation, which makes it more convenient to characterize structures including both differential and single-ended ports like printed circuit boards with multiple traces and vias (paper 4).

## PAPER

### **I. An Improved Dipole-Moment Model Based on Near-Field Scanning for Characterizing Near-Field Coupling and Far-Field Radiation from an IC**

Zhenwei Yu, *Student Member, IEEE*, and Jun Fan, *Senior Member, IEEE*

*Abstract*—In this paper, an improved dipole-moment model for characterizing near-field coupling and far-field radiation from an IC based on near-field scanning is proposed. An array of electric and magnetic dipole moments is used to reproduce the field distributions in a scanning plane above an IC. These dipole moments can then be used as noise sources for the IC. In order to ensure the accurate prediction of the near-field coupling from the IC, the regularization technique and the truncated singular-value decomposition (SVD) method are investigated in this paper, together with the conventional least square method, to reconstruct the dipole moments from the near-field scanning data. A simple example is used to demonstrate the approach. The improved dipole-moment model is particularly useful for addressing radio-frequency interference (RFI) issues where near-field noise coupling needs to be accurately analyzed.

*Index Terms*—Dipole-moment model, regularization technique, truncated singular-value decomposition (SVD) method, near-field scanning, near-field coupling, radio-frequency interference (RFI).

#### I. INTRODUCTION

Electromagnetic Compatibility (EMC) of integrated circuits (ICs) is becoming an increasingly important aspect in high-speed circuit designs [1]. International standards have been established to quantify the emission and immunity performance of ICs using

various measurement methods [2], [3]. Further, IC-EMC models are desirable for system-level EMC predictions. These models may be obtained from simulations when sufficient IC information is available [4]-[8]. However, in most practical cases, detailed IC information may not be available to system and printed circuit board (PCB) designers. Thus, IC-EMC models extracted from measurements become more attractive in this situation.

For radiated emissions from an IC, many research efforts have been focused on the development of an equivalent model from near-field scanning. In [9]-[13], some equivalent magnetic or/and electric current sources were calculated according to Huygens' equivalence principle at the near-field scanning plane, and used to estimate the near- and far-field above the scanning plane. Obviously, this approach cannot allow an observation point located below the scanning plane, which may not be an issue for radiated EMI. However, for radio-frequency interference (RFI) issues in mixed RF/digital systems, interference from digital ICs to RF subsystems is often through near-field coupling where the victims may not be located above a practical scanning plane. In this case, the approach becomes insufficient. An alternative source reconstruction method was proposed in [14] and [15], with equivalent electric and magnetic current sources calculated at a source reconstruction plane, which is lower than the near-field scanning plane but higher than the IC under measurement. Unfortunately these equivalent sources are still located outside of the IC, and thus may not be able to accurately reflect the current and voltage distributions inside the IC. Electric and magnetic dipoles were used as noise sources in [16]-[19]. They were horizontally placed in the location of the IC, to characterize its radiated emissions. In [20]-[22], these dipoles were imported into a



commercial full-wave simulation tool for system-level simulations. However, these noise sources were obtained using the least square method, a conventional approach to solve the inverse problem of source reconstruction. Due to the ill-posed transformation matrix relating the equivalent sources and the measured near-field data, the solution is very sensitive to noise and is not unique. It will be shown later in this paper that some possible solutions may give incorrect near field estimation when an observation point is located near the IC.

Some optimization algorithms were further developed to reconstruct the equivalent dipoles from near-field scanning data [23]-[25]. The number of the dipoles can be minimized in the frequency range of interest and their locations can be determined. In some other studies, equivalent source models were constructed with available geometrical information of the IC [26]. The available information could be used to ensure the accuracy of the reconstructed source models.

In this paper, noise source model for an IC located on a large ground plane based on near-field scanning is studied and improved for accurate field evaluations in both the near- and far-field regions. No geometrical information about the IC under study is assumed. To achieve the objective, a different set of the dipole sources compared to [16]-[22] are adopted to better reflect the possible voltage and current distributions in the IC. It will be demonstrated later that vertical electric dipoles  $Pz$  are used to describe the voltage distribution while horizontal magnetic dipoles  $Mx$  and  $My$  describe the current distribution. The magnitudes and phases of the dipoles are calculated using the least square method combined with the regularization technique [27]-[30], in order to eliminate potential false solutions and ensure the accuracy in near-field estimations. The

equivalent sources are placed above the ground plane near the IC to replace the actual IC for system-level EMC simulations. When the equivalent sources are extracted, the effect of the ground plane is excluded in the dipole models. This is necessary when the dipole models are used in system-level simulations; otherwise multiple-scattering effect between the ground plane and other scatters may not be properly accounted for.

The electromagnetic fields of dipole moments are briefly reviewed in Section II. In Section III, the least square method with the regularization technique is introduced. An alternative approach using the truncated singular value decomposition (SVD) method is also discussed and demonstrated to be equivalent to the regularization method. Validations and discussions for the improved dipole-moment model are presented in Section IV, followed by conclusions in Section V.

## II. ELECTROMAGNETIC FIELDS OF DIPOLE MOMENTS

According to the multi-pole expansion of an electromagnetic radiation source [31], an arbitrary electrically small source can be approximately replaced by six dipoles: three electric dipoles denoted  $P_x$ ,  $P_y$ , and  $P_z$ , and three magnetic dipoles denoted  $M_x$ ,  $M_y$ , and  $M_z$ . These dipoles together generate approximately the same field as the source. A finite-sized source can be segmented into a number of electrically small ones, and therefore can be approximately modeled as an array of electric and magnetic dipoles.

Assume an IC above a large ground plane can be modeled as  $N \times N$  electrically small sources. Then, each of these electrically small sources can be further replaced with a set of dipoles. As mentioned earlier, these dipoles are located at the ground plane as shown in Fig. 1. Notice that, because of the large ground plane, only three out of the six dipole moments are needed in each cell:  $M_x$ ,  $M_y$ , and  $P_z$  in the x-, y-, and z-directions,

respectively. When the IC is very close to the ground plane, the perfect electric conductor (PEC) boundary condition determines that these three dipole moments dominate. Further, the three dipole moments represent the dominant voltage and current distributions in the IC. It will be shown later that the voltage distribution between IC traces and the ground plane can be modeled by  $P_z$ , and the current distribution can be modeled by  $M_x$  and  $M_y$ .

The electromagnetic fields generated by these three dipoles in the half space above an infinite ground plane can be derived analytically [31], [32]. Assume the dipoles are located at  $(x', y', d)$ , where  $d$  is greater than zero and represents the height of dipoles above the ground plane. The tangential electric and magnetic fields at the observation point  $(x, y, z)$  can be found as

$$E_x = \tau_E \left\{ \left[ \frac{(z-d)(x-x')}{r_1^2} q_1(r_1) + \frac{(z+d)(x-x')}{r_2^2} q_1(r_2) \right] P_z + \left[ \frac{(z-d)}{r_1} q_3(r_1) + \frac{(z+d)}{r_2} q_3(r_2) \right] k_0 M_y \right\} \quad (1)$$

$$E_y = \tau_E \left\{ \left[ \frac{(y-y')(z-d)}{r_1^2} q_1(r_1) + \frac{(y-y')(z+d)}{r_2^2} q_1(r_2) \right] P_z + \left[ -\frac{(z-d)}{r_1} q_3(r_1) - \frac{(z+d)}{r_2} q_3(r_2) \right] k_0 M_x \right\} \quad (2)$$

$$H_x = \tau_H \left\{ -\left[ \frac{(y-y')}{r_1} q_3(r_1) + \frac{(y-y')}{r_2} q_3(r_2) \right] P_z + \left[ -\frac{(y-y')^2 + (z-d)^2}{r_1^2} q_1(r_1) + q_2(r_1) - \frac{(y-y')^2 + (z+d)^2}{r_2^2} q_1(r_2) + q_2(r_2) \right] k_0 M_x + \left[ \frac{(x-x')(y-y')}{r_1^2} q_1(r_1) + \frac{(x-x')(y-y')}{r_2^2} q_1(r_2) \right] k_0 M_y \right\} \quad (3)$$

$$\begin{aligned}
H_y = \tau_{II} \left\{ \left[ \frac{(x-x')}{r_1} q_3(r_1) + \frac{(x-x')}{r_2} q_3(r_2) \right] P_z \right. \\
+ \left[ \frac{(x-x')(y-y')}{r_1^2} q_1(r_1) + \frac{(x-x')(y-y')}{r_2^2} q_1(r_2) \right] k_0 M_x \\
+ \left[ -\frac{(z-d)^2 + (x-x')^2}{r_1^2} q_1(r_1) + q_2(r_1) \right. \\
\left. \left. - \frac{(z+d)^2 + (x-x')^2}{r_2^2} q_1(r_2) + q_2(r_2) \right] k_0 M_y \right\} \quad (4)
\end{aligned}$$

where  $\tau_{II} = -j \frac{k_0 \eta_0}{4\pi}$  and  $\tau_{II} = \frac{k_0}{4\pi}$ ;  $k_0$  is the free space wave number;  $\eta_0$  is the wave

impedance in vacuum;  $P_z$  is a complex number denoting the electric dipole moment in the unit of  $A \cdot m$ ;  $M_x$  and  $M_y$  denoting the magnetic dipole moments in the unite of  $A \cdot m^2$ .

The terms  $r_1$  and  $r_2$  can be written as

$$r_1 = \left[ (x-x')^2 + (y-y')^2 + (z-d)^2 \right]^{1/2} \quad (5)$$

$$r_2 = \left[ (x-x')^2 + (y-y')^2 + (z+d)^2 \right]^{1/2} \quad (6)$$

They are actually the distances from the observation point to the three dipoles and their images, respectively. By using the images assuming the ground plane is large enough, the effect of the ground plane is considered in the field calculations but not included in the dipole moments. This is important as discussed earlier. The ground plane should not be included in the dipole moments; otherwise, multiple scattering between the ground plane and other scatters in a later on system-level simulation cannot be accounted for. The terms  $q_1(r)$ ,  $q_2(r)$ , and  $q_3(r)$  can be written as

$$q_1(r) = \left[ \frac{3}{(k_0 r)^2} + j \frac{3}{k_0 r} - 1 \right] f(r) \quad (7)$$

$$q_2(r) = \left[ \frac{2}{(k_0 r)^2} + j \frac{2}{k_0 r} \right] f(r) \quad (8)$$

$$q_3(r) = \left[ \frac{1}{k_0 r} + j \right] f(r) \quad (9)$$

where

$$f(r) = \frac{e^{-jk_0 r}}{r} \quad (10)$$

According to (1)-(4), the electromagnetic fields excited by the IC are the total contributions of all the dipoles, and can be calculated as

$$\begin{pmatrix} [E_x]_{M^2 \times 1} \\ [E_y]_{M^2 \times 1} \\ [H_x]_{M^2 \times 1} \\ [H_y]_{M^2 \times 1} \end{pmatrix} = T \begin{pmatrix} [P_z]_{N^2 \times 1} \\ [M_x]_{N^2 \times 1} \\ [M_y]_{N^2 \times 1} \end{pmatrix} \quad (11)$$

where  $[E_x]$ ,  $[E_y]$ ,  $[H_x]$ , and  $[H_y]$  are the x- and y-directional components of the electric and magnetic fields; the number of the measurement points in the near-field scanning measurement is assumed to be  $M \times M$ ;  $[P_z]$ ,  $[M_x]$ , and  $[M_y]$  are the electric and magnetic dipole moments in the equivalent dipole array; and,  $T$  is the transformation matrix and can be written as

$$T = \begin{pmatrix} T_{ExPz} & T_{ExMx} & T_{ExMy} \\ T_{EyPz} & T_{EyMx} & T_{EyMy} \\ T_{HxPz} & T_{HxMx} & T_{HxMy} \\ T_{HyPz} & T_{HyMx} & T_{HyMy} \end{pmatrix}. \quad (12)$$

Each submatrix in (12) has a size of  $M^2 \times N^2$ , and represents the contributions of one sort of dipoles to one field component, e. g.,  $T_{ExPz}$  describes the  $E_x$  field components generated by all the  $P_z$  dipoles in the array. The elements of each submatrix can be calculated as

$$T_{Expz}(i, j) = \tau_E \left[ \frac{(z(i) - d)(x(i) - x'(j))}{r_1(i, j)^2} q_1(r_1(i, j)) + \frac{(z(i) + d)(x(i) - x'(j))}{r_2(i, j)^2} q_1(r_2(i, j)) \right] \quad (13)$$

$$T_{EMx} = 0 \quad (14)$$

$$T_{EMy} = \tau_E \left[ \frac{(z(i) - d)}{r_1(i, j)} q_3(r_1(i, j)) + \frac{(z(i) + d)}{r_2(i, j)} q_3(r_2(i, j)) \right] k_0 \quad (15)$$

$$T_{Eypz}(i, j) = \tau_E \left[ \frac{(y(i) - y'(j))(z(i) - d)}{r_1(i, j)^2} q_1(r_1(i, j)) + \frac{(y(i) - y'(j))(z(i) + d)}{r_2(i, j)^2} q_1(r_2(i, j)) \right] \quad (16)$$

$$T_{Eymx}(i, j) = \tau_E \left[ -\frac{(z(i) - d)}{r_1(i, j)} q_3(r_1(i, j)) - \frac{(z(i) + d)}{r_2(i, j)} q_3(r_2(i, j)) \right] k_0 \quad (17)$$

$$T_{Eymy}(i, j) = 0 \quad (18)$$

$$T_{Hxpz} = -\tau_H \left[ \frac{(y(i) - y'(j))}{r_1(i, j)} q_3(r_1(i, j)) + \frac{(y(i) - y'(j))}{r_2(i, j)} q_3(r_2(i, j)) \right] \quad (19)$$

$$T_{Hxm} = \tau_H \left[ -\frac{(y(i) - y'(j))^2 + (z(i) - d)^2}{r_1(i, j)^2} q_1(r_1(i, j)) + q_2(r_1(i, j)) - \frac{(y(i) - y'(j))^2 + (z(i) + d)^2}{r_2(i, j)^2} q_1(r_2(i, j)) + q_2(r_2(i, j)) \right] k_0 \quad (20)$$

$$T_{Hxmy} = \tau_H \left[ \frac{(x(i) - x'(j))(y(i) - y'(j))}{r_1(i, j)^2} q_1(r_1(i, j)) + \frac{(x(i) - x'(j))(y(i) - y'(j))}{r_2(i, j)^2} q_1(r_2(i, j)) \right] k_0 \quad (21)$$

$$T_{Hypz} = \tau_H \left[ \frac{(x(i) - x'(j))}{r_1(i, j)} q_3(r_1(i, j)) + \frac{(x(i) - x'(j))}{r_2(i, j)} q_3(r_2(i, j)) \right] \quad (22)$$

$$T_{Hymx} = \tau_H \left[ \frac{(x(i) - x'(j))(y(i) - y'(j))}{r_1(i, j)^2} q_1(r_1(i, j)) + \frac{(x(i) - x'(j))(y(i) - y'(j))}{r_2(i, j)^2} q_1(r_2(i, j)) \right] k_0 \quad (23)$$

$$T_{HyMy} = \tau_H \left[ -\frac{(z(i)-d)^2 + (x(i)-x'(j))^2}{r_1(i,j)^2} q_1(r_1(i,j)) + q_2(r_1(i,j)) - \frac{(z(i)+d)^2 + (x(i)-x'(j))^2}{r_2(i,j)^2} q_1(r_2(i,j)) + q_2(r_2(i,j)) \right] k_0 \quad (24)$$

where  $i$  is the index of an observation location ( $1 \leq i \leq M^2$ );  $j$  is the index of a dipole source location ( $1 \leq j \leq N^2$ );  $x(i)$ ,  $y(i)$ , and  $z(i)$  are the coordinates of the observation point;  $x'(j)$  and  $y'(j)$  are the horizontal coordinates of the dipole source location;  $r_1(i, j)$  and  $r_2(i, j)$  are defined as

$$r_1(i, j) = \left[ (x(i) - x'(j))^2 + (y(i) - y'(j))^2 + (z(i) - d)^2 \right]^{1/2} \quad (25)$$

$$r_2(i, j) = \left[ (x(i) - x'(j))^2 + (y(i) - y'(j))^2 + (z(i) + d)^2 \right]^{1/2} \quad (26)$$

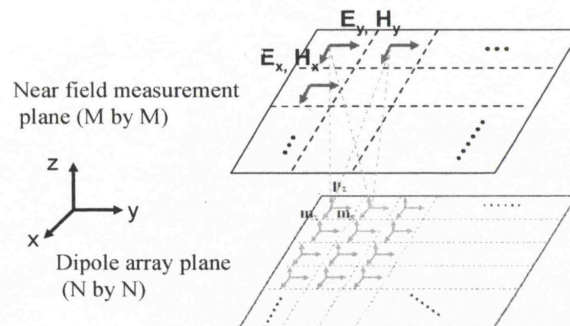


Fig. 1. Equivalent source model using a dipole array.

### III. DIPOLE MODEL EXTRACTION

Equation (11) needs to be solved to obtain the equivalent dipoles from the near-field scanning data, a typical inverse problem. First of all, the field data in (11) is normalized as

$$F_n = \begin{bmatrix} [E_x]_{M^2,1} / E_{\max} \\ [E_y]_{M^2,1} / E_{\max} \\ [H_x]_{M^2,1} / H_{\max} \\ [H_y]_{M^2,1} / H_{\max} \end{bmatrix} \quad (27)$$

where subscript  $n$  stands for normalization; and,  $E_{\max}$  and  $H_{\max}$  are the maximum values of the tangential electric and magnetic fields, which can be defined as

$$E_{\max} = \max\{\max(|E_x|), \max(|E_y|)\} \quad (28)$$

$$H_{\max} = \max\{\max(|H_x|), \max(|H_y|)\} \quad (29)$$

The equivalent sources in (11) are also normalized as

$$X_k \equiv \begin{pmatrix} [P_z]_{N^2,1} \\ [k_0 M_x]_{N^2,1} \\ [k_0 M_y]_{N^2,1} \end{pmatrix} \quad (30)$$

where the subscript  $k$  denotes the normalization with regard to  $k_0$ . These normalizations are needed to result in a better matrix condition, and thus a more accurate solution in the inverse problem. Substituting (27) and (30) into (11) results in

$$F_n = T_{nk} X_k \quad (31)$$

where

$$T_{nk} = \begin{bmatrix} T_{ExPz} / E_{\max} & T_{ExMx} / (E_{\max} k_0) & T_{ExMy} / (E_{\max} k_0) \\ T_{EyPz} / E_{\max} & T_{EyMx} / (E_{\max} k_0) & T_{EyMy} / (E_{\max} k_0) \\ T_{HxPz} / H_{\max} & T_{HxMx} / (H_{\max} k_0) & T_{HxMy} / (H_{\max} k_0) \\ T_{HyPz} / H_{\max} & T_{HyMx} / (H_{\max} k_0) & T_{HyMy} / (H_{\max} k_0) \end{bmatrix} \quad (32)$$

The conventional least square method minimizes an objective function  $H_1$ , which is defined as

$$H_1 = \|F_n - T_{nk} X_k\|^2, \quad (33)$$

and the least square solution is given by



$$X_k = [T_{nk} \quad T_{nk}']^{-1} T_{nk}' F_n \quad (34)$$

where  $T_{nk}'$  denotes the conjugate transpose of  $T_{nk}$ .

To facilitate further discussions, an example is given and the least square method is employed to solve the inverse problem. As shown in Fig. 2, a trace with an open patch is constructed in a full-wave simulation tool [33]. The trace is 1 mil thick and 10 mils above a ground plane with dimensions of  $2000 \times 2000$  mils. The entire structure is in the free space. The trace has a width of 40 mils and a length of 1200 mils. An 80 mil by 80 mil patch is added near the source region. The trace is excited by a voltage source of one volt with a source impedance of 50 ohms, and terminated by a 50-ohm load.

Simulated near-field data are obtained at an 800 mil by 800 mil plane, which is 50 mils above the ground plane shown in Fig. 2, with a pitch size of 20 mils along both the x- and y-directions. The source region has dimensions of 620 x 620 mils, covered with dipole sets with a pitch size of 20 mils at both directions as well. The dipoles are half way between the trace and the ground, i.e., 5 mils above the ground plane. Using the least square method, the dipole moments are calculated from the simulated near-field data and are plotted in Fig. 3. These dipoles can generate similar field at the scanning plane as the original trace/patch structure, but it is clearly seen that they do not reflect the voltage and current distributions in the example geometry at all. This solution, as demonstrated later, is fine to calculate the fields relatively far away from the source, but could result in errors in certain near-field evaluations.

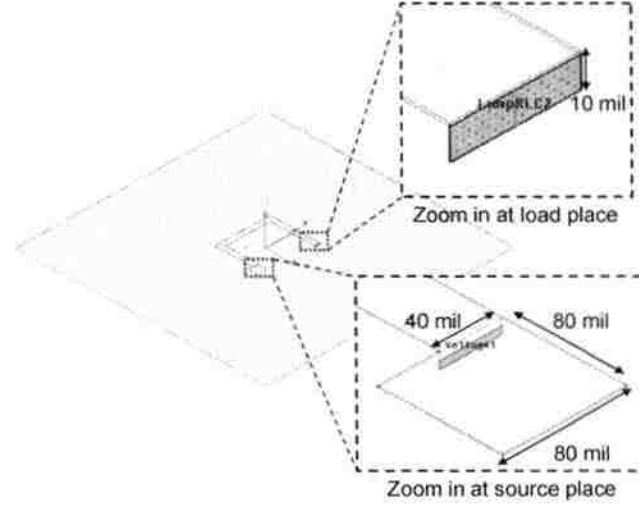


Fig. 2. Geometry of an example.

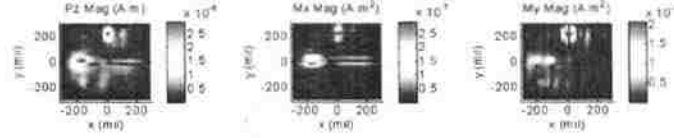


Fig. 3. Equivalent sources calculated using the conventional least square method.

#### A. Regularization Technique

The regularization technique is proposed to solve the inverse problem in (11). The objective function to be minimized is re-defined as

$$H = \|F_n - T_{nk} X_k\|^2 + \lambda^2 \|X_k\|^2 \quad (35)$$

where  $\lambda$  is a regularization coefficient. The first term  $\|F_n - T_{nk} X_k\|^2$  in  $H$  determines the accuracy of the solution, and the second term  $\lambda^2 \|X_k\|^2$  tries to minimize the total energy of the equivalent sources. The solution that minimizes  $H$  can be written as

$$X_k^{reg}(\lambda) = [T_{nk}' T_{nk} + \lambda^2 I]^{-1} T_{nk}' F_n \quad (36)$$

where superscript *reg* denotes a solution using the regularization technique; and,  $I$  is an identity matrix. The regularization coefficient  $\lambda$  is used to adjust the weights of the two terms (in other words, two different constraints). Several methods have been proposed for

selecting  $\lambda$  [29], [30]. In this work,  $\lambda$  is selected according a discrepancy principle proposed in [34].

Specifically, a relative error between the scanned (in this example simulated) fields in the scanning plane and the fields generated by the equivalent dipole sources in the same plane is defined as

$$Er_{\text{Model}}(\lambda) = \frac{\|F_n - T_{nk} X_k^{\text{reg}}(\lambda)\|}{\|F_n\|} \quad (37)$$

where  $\|F_n\|$  denotes the norm of the fields, which can be written as

$$\|F_n\| = \sqrt{\sum_{i,j} \left[ \left( \frac{E_x(i,j)}{E_{\max}} \right)^2 + \left( \frac{E_y(i,j)}{E_{\max}} \right)^2 + \left( \frac{H_x(i,j)}{H_{\max}} \right)^2 + \left( \frac{H_y(i,j)}{H_{\max}} \right)^2 \right]} \quad (38)$$

where  $(i, j)$  is the index of the field observation point in the scanning plane. Equation (37) indicates that the relative error changes with  $\lambda$ . The error reaches its minimum value when  $\lambda = 0$ . Then, a proper value of  $\lambda$  can be determined by

$$Er_{\text{Model}}(\lambda) = Er_{\text{data}} \quad (39)$$

$Er_{\text{data}}$  denotes the data error in scanning measurements or in simulation in this case.

which can be estimated based on experience. An iterative algorithm is designed to search for the  $\lambda$  satisfying (39).

To demonstrate the effectiveness of the regularization technique, the same example structure shown in Fig. 2 is studied again. The dipole moments calculated from (36) are plotted in Fig. 4. It can be clearly seen that the  $P_z$  dipoles are mainly distributed along the trace as well as the patch near the source. They reflect the voltage distribution. Notice that, although the patch is open, there's still voltage difference to the ground plane. The  $M_y$  dipoles are mainly distributed along the y-directional part of the trace. They

reflect the current flow in the y-direction. Similarly, the  $M_y$  dipoles are mainly distributed at the x-directional parts of the trace. Notice that there are no magnetic dipoles in the patch region, because there's no current since the patch is open. Using the regularization approach, the extract dipole moments agree better with the physical voltage and current distributions. Consequently they can result in a better accuracy in near-field evaluations.

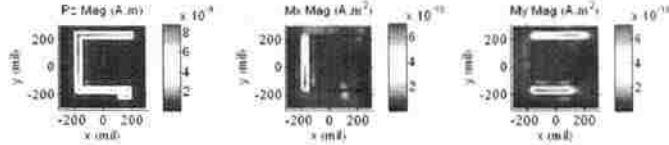


Fig. 4. Improved dipole-moment model extracted using the regularization technique.

#### B. Truncated Singular-Value Decomposition (SVD) Method

An alternative approach to the regularization technique is the truncated SVD method, which is based on the singular-value decomposition of the matrix  $T_{nk}$  in (32) as

$$T_{nk} = USV' \quad (40)$$

where  $V'$  denotes the conjugate transpose of  $V$ ; and,  $U$  and  $V$  are  $K \times K$  and  $L \times L$  unitary matrices, i.e.,  $U' = U^{-1}$ ,  $V' = V^{-1}$ . It should be noted that  $T_{nk}$  is a  $K$  by  $L$  matrix ( $K > L$ ) and the rank of  $T_{nk}$  is  $L$ .  $S$  is a  $K$  by  $L$  matrix which can be written as

$$S = \begin{bmatrix} s_{11} & 0 & 0 \\ 0 & \ddots & 0 \\ 0 & 0 & s_{LL} \\ \vdots & \vdots & \vdots \\ 0 & 0 & 0 \end{bmatrix}_{K \times L} \quad (41)$$

where  $s_{11} \geq s_{22} \cdots \geq s_{LL} \geq 0$ . These diagonal elements are the singular-values of  $T_{nk}$ . The least square solution of (31) can be written as

$$X_k^{LS} = \left[ T_{nk}' T_{nk} \right]^{-1} T_{nk}' F_n \quad (42)$$

where  $X_k^{LS}$  is an  $L \times 1$  vector; superscript  $LS$  denotes the least square solution; and,  $F_n$  is a  $K \times 1$  vector. Substituting (40) and (41) into (42) yields

$$X_k^{LS} = V \begin{bmatrix} s_{11}^{-1} & & \\ & \ddots & \\ & & s_{LL}^{-1} \end{bmatrix} U_L' F_n \quad (43)$$

where  $U_L$  is the first  $L$  columns of  $U$ , and therefore  $U_L'$  is an  $L \times K$  matrix.  $F_n$  is the scanned field data and usually includes noise. According to (43),  $X_k^{LS}$  could be significantly affected by the noise when some of the singular values are small.

In order to eliminate this noise issue, the small singular values can be set to zero.

In other words, the solution can be rewritten as

$$X_k^{TSVD}(r) = V_r \begin{bmatrix} s_{11}^{-1} & & \\ & \ddots & \\ & & s_{rr}^{-1} \end{bmatrix} U_r' F_n \quad (44)$$

where  $V_r$  is an  $L \times r$  matrix generated from the first  $r$  columns of  $V$ ;  $U_r$  is a  $K \times r$  matrix generated from the first  $r$  columns of  $U$ ,  $X_k^{TSVD}(r)$  is an  $L \times 1$  vector; superscript  $TSVD$  denotes the solution by the truncated SVD method; and,  $r$  is the number of the larger singular values that are kept unchanged. Again, the discrepancy principle proposed in [33] can be used to decide the value of  $r$ . In this work,  $r$  is selected from the following procedures. Similar to (37), a relative error is defined as

$$Er_{\text{Model}}(r) = \frac{\|F_n - T_{nk} X_k^{TSVD}(r)\|}{\|F_n\|} \quad (45)$$

When  $r = L$ , the relative error reaches its minimum value. Similar to (39),  $r$  can be determined by

$$Er_{\text{Model}}(r) = Er_{\text{Data}} \quad (46)$$

where  $Er_{Data}$  denotes the data error in the near-field scanning.

This method is also employed to the same example shown in Fig. 2. The dipole moments calculated from (44) are plotted in Fig. 5. Similar results are obtained as by the regularization technique in Fig. 4.

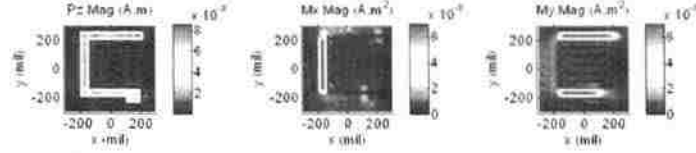


Fig. 5. Improved dipole moment model extracted using the truncated SVD approach.

### C. Relationship between Regularization and Truncated SVD Approaches

The regularization and truncated SVD approaches can be related mathematically. According to the singular-value decomposition of  $T_{nk}$  in (40), the equivalent sources by the regularization technique in (36) can be rewritten as

$$X_k^{reg} = V \begin{bmatrix} \frac{s_{11}}{s_{11}^2 + \lambda^2} & & & \\ & \ddots & & \\ & & \frac{s_{ll}}{s_{ll}^2 + \lambda^2} & \\ & & & \ddots \end{bmatrix} U_l^T F_n \quad (47)$$

For an integer  $l$ ,  $1 \leq l \leq L$ , if  $s_{ll}$  is much less than  $\lambda$ ,  $\frac{s_{ll}}{s_{ll}^2 + \lambda^2}$  approximately equals to 0; if  $s_{ll}$  is much larger than  $\lambda$ ,  $\frac{s_{ll}}{s_{ll}^2 + \lambda^2}$  approximately equals to  $s_{ll}^{-1}$ . Therefore,

$\lambda$  has almost no influence on the diagonal terms related to larger singular values, but makes the terms with smaller singular values zero. The contribution of the regularization coefficient  $\lambda$  is to gradually truncate the singular-values in the diagonal matrix. In this sense, the two approaches are equivalent.

#### IV. VALIDATION AND DISCUSSIONS

The improved dipole-moment model extracted using the regularization technique is validated in a 100-mil-high plane as well as at some far-field locations, as shown in Fig. 6. The far-field observation points are at  $r = 3 \text{ m}$  away from the origin point with  $\theta = 89 \text{ degrees}$  and  $\phi$  from  $0$  to  $360 \text{ degrees}$ . As shown in Fig. 7, the fields from the improved dipole-moment sources can reproduce those from the original structure calculated using a full-wave tool.

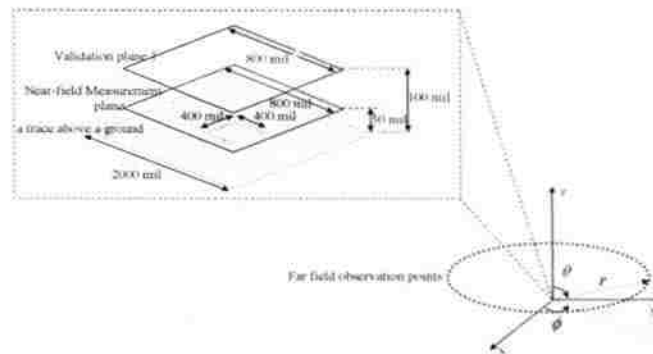
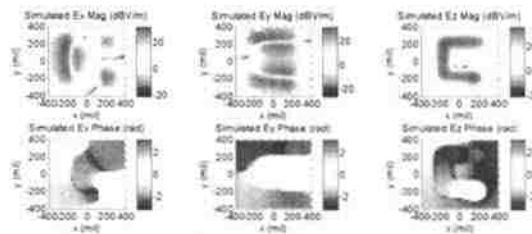


Fig. 6. Validation: near-field scanning plane, 100-mil-high validation plane, and 3 meter far-field observation points.



(a) E-field distribution from the original structure at 100 mils above the ground plane.

Fig. 7. Validation of the improved dipole-moment sources.

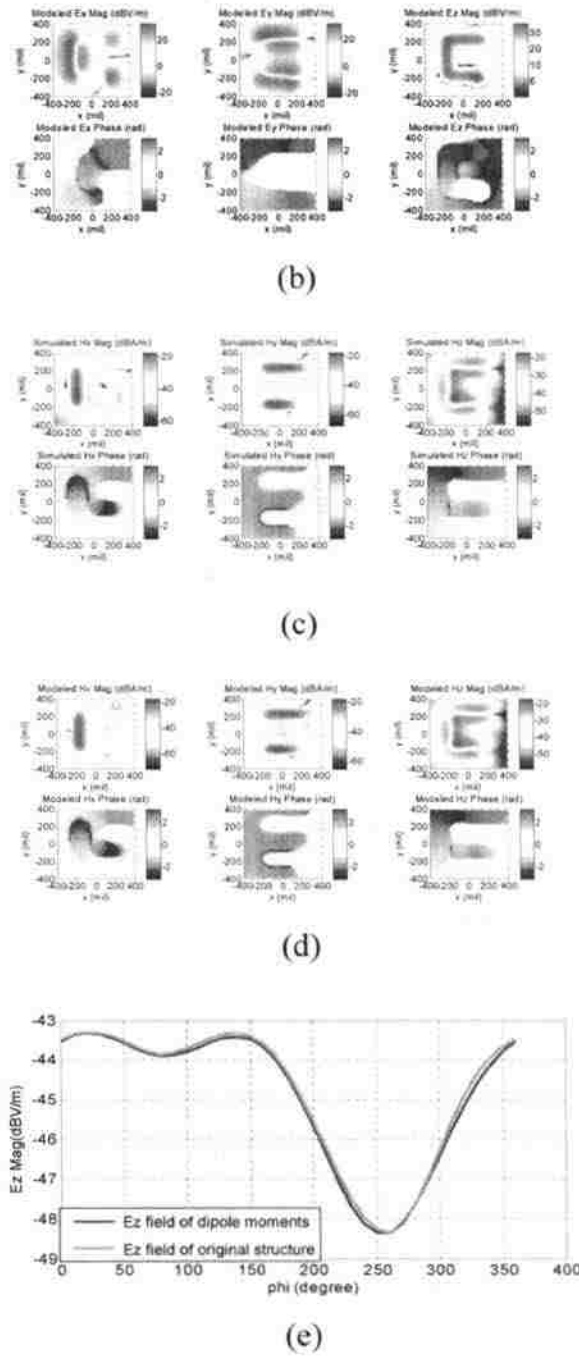


Fig. 7. Cont. Validation of the improved dipole-moment sources. (b) E-field distribution calculated from the improved dipole-moment sources at 100 mils above the ground plane; (c) H-field distribution from the original structure at 100 mils above the ground plane; (d) H-field distribution calculated from the improved dipole-moment sources at 100 mils above the ground plane; (e) magnitudes of  $E_z$  at the far-field observation points 3 meters away.



As discussed earlier, the direct solution from the least square method may introduce errors in certain near-field evaluations. Let's take the same example, and compare the fields in a plane 30-mils above the ground plane. Notice that this plane is below the near-field scanning plane. The fields from the original structure, from the improved dipole-moment sources extracted using the regularization techniques, and from the dipole moments extracted using the conventional least square method are compared in Fig. 8, where the fields are evaluated along the  $y = 0$  axis. It can be clearly seen that the improved dipole-moment sources extracted using the regularization method can predict the fields correctly even at a height lower than the near-field scanning plane, while the dipole moments extracted using the conventional least square method introduces significant errors. This simple example demonstrates the effectiveness of the improved

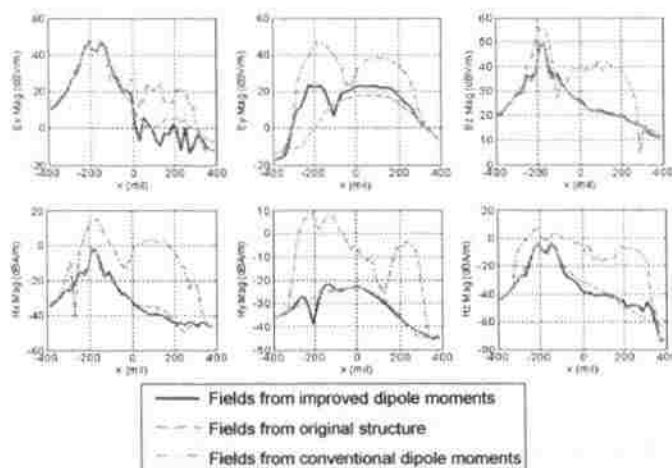


Fig. 8. Comparisons of the field magnitudes along the  $y=0$  axis at the plane 30 mils above the ground plane from the original structure, from the improved dipole-moment sources extracted from the regularization technique, and from the dipole moments extracted from the conventional least square method.

model proposed in this work for RFI applications, where the victims may be located close to the aggressor IC below the possible scanning plane in practical cases.

As mentioned earlier, the dipole moments extracted using the regularization or the truncated SVD approach could reflect the voltage and current distributions in the IC under study. This can be further demonstrated quantitatively. As shown Fig. 9, the electric charge on one small segment of the trace surface can be calculated as

$$Q = VC'_N \quad (48)$$

where  $V$  is the voltage of the trace segment relative to the ground plane;  $C'_N$  is the capacitance between the trace segment and the ground plane; and,  $\Delta l$  is the length of the segment. As illustrated in Fig. 10, since the current flowing through the capacitance is

$$I_{ch} = \frac{dQ}{dt} = j\omega Q \quad (49)$$

The electric dipole moment relating the voltage in this trace segment can be then calculated as

$$P_z = I_{ch} h = j\omega Qh \quad (50)$$

where  $j$  is the imaginary unit;  $\omega$  is the working angular frequency; and,  $h$  is the spacing between the trace and the ground plane. The capacitance  $C'_N$  can be written as

$$C'_N = \frac{k' \varepsilon w \Delta l}{h} \quad (51)$$

where  $w$  is the width of the trace;  $\varepsilon$  is the permittivity of the medium; and,  $k'$  is a factor used to take into account the fringing effect. According to (48), (50), and (51), the electric dipole moment  $P_z$  for the segment can be calculated as

$$P_z = j\omega C'_N Vh \quad (52)$$

The magnitude of  $P_z$  is proportional to the magnitude of the voltage  $V$ , while its phase is  $\frac{\pi}{2}$  ahead of the voltage.

As shown in Fig. 11, the magnetic dipole moment for a trace segment can be calculated from the current flowing through the segment as

$$M = Ih\Delta l \quad (53)$$

where  $I$  is the current flowing through the segment; and,  $h$  is the spacing between the trace and the ground plane. Therefore the magnetic dipole moment is proportional to and has the same phase as the current  $I$ .

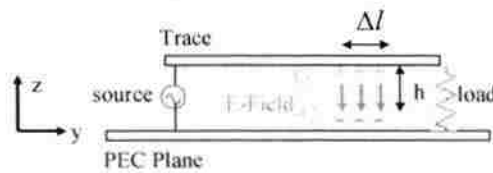


Fig.9. Charge on the trace and the ground plane due to a potential difference.

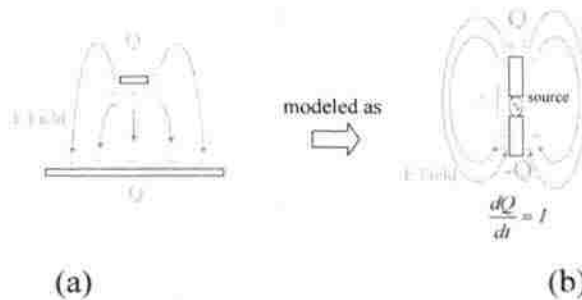


Fig. 10. Calculation of an electric dipole moment: (a) charge distribution and electric field; (b) equivalent electric dipole.

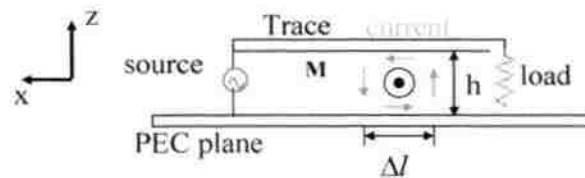


Fig. 11. Calculation of a magnetic dipole moment.

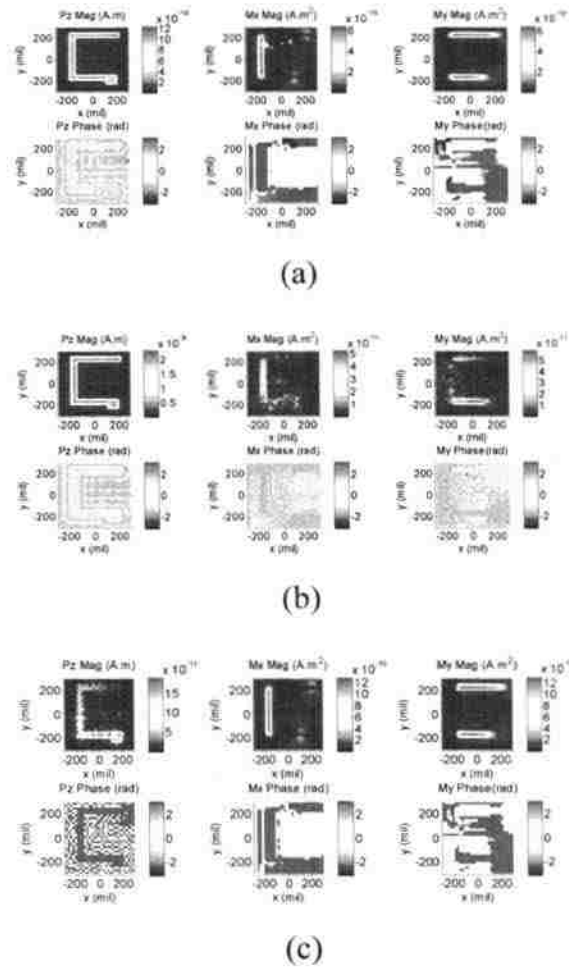


Fig. 12. Dipole moments extracted using the regularization technique for the test geometry shown in Fig. 2 at 100 MHz, when the trace is (a) matched; (b) open ended; and, (c) short ended.

The same test geometry shown in Fig. 2 is studied with three different terminations: matched, open, and short. The voltage and current along the trace can be calculated using the transmission line theory. Then electric and magnetic dipole moments can be estimated based on the voltage and current information using (52) and (53).

Meanwhile, the three cases are simulated in a full-wave tool to obtain the fields in the scanning plane. Then, the regularization technique is applied to extract the dipole moments. The distributions of the dipole moments are shown in Fig. 12. It is worth

pointing out that the distributions of the dipole moments along the trace, when it is open or short ended, exhibit the standing wave patterns. This again demonstrates that the proposed method can achieve a better source model that reflects the actual physics.

The dipole moments at the middle of the y-directional part of the trace estimated from the voltage/current information are compared to those extracted using the regularization technique in Table I. In general, the results agree well, which reveals the relationships between the dipole moments and the voltage/current distributions.

TABLE I. COMPARISONS OF DIPOLE MOMENTS.

Load condition		Dipole moments	
		Extracted using regularization	From voltage and current information
Matched	E-dipole ( $A \cdot m$ )	$2.3 \times 10^{-9}$	$2.4 \times 10^{-9}$
	H-dipole ( $A \cdot m^2$ )	$1.4 \times 10^{-9}$	$1.3 \times 10^{-9}$
Open	E-dipole ( $A \cdot m$ )	$4.7 \times 10^{-9}$	$4.8 \times 10^{-9}$
	H-dipole ( $A \cdot m^2$ )	$7.2 \times 10^{-11}$	$8.2 \times 10^{-11}$
Short	E-dipole ( $A \cdot m$ )	$2.0 \times 10^{-10}$	$1.6 \times 10^{-10}$
	H-dipole ( $A \cdot m^2$ )	$2.8 \times 10^{-9}$	$2.6 \times 10^{-9}$

## V. EXPERIMENTAL VALIDATION

The physical dipole model is validated experimentally as well. A circuit is built on a PCB (Printed Circuit Board) as shown in Fig. (a), and considered as a radiating source like an IC. The signal transmitted in the circuit is an 80 MHz clock signal. The dimension of the board is 120 mm by 120 mm, and sits at a large metal plane when scanning. The scanning area is 3.1 mm above the ground plane, the area is 250 mm by

290 mm, and the scanning area is 5 mm spacing. The metal plane can be considered as an infinite ground plane compared with the dimension of the circuit board and the scanning area. Electric and magnetic fields are obtained at the scanning plane using a near-field scanning system, and plotted in Fig. (b).

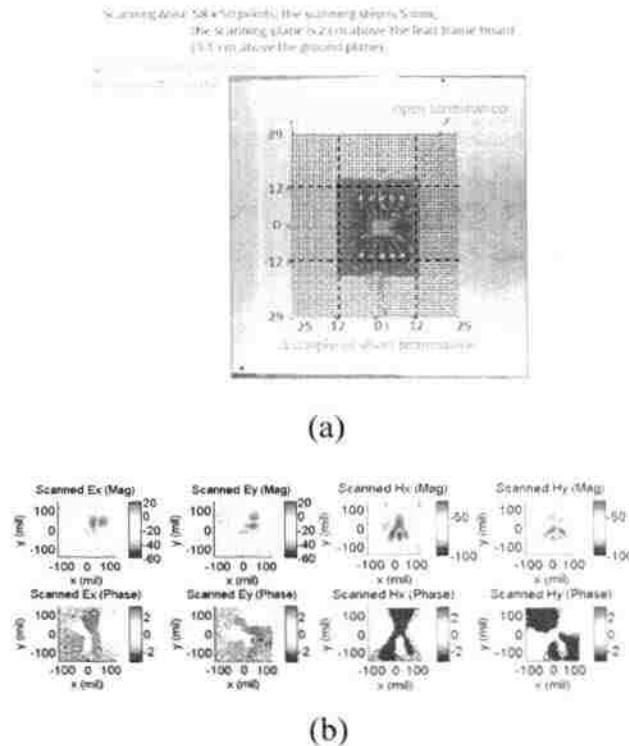


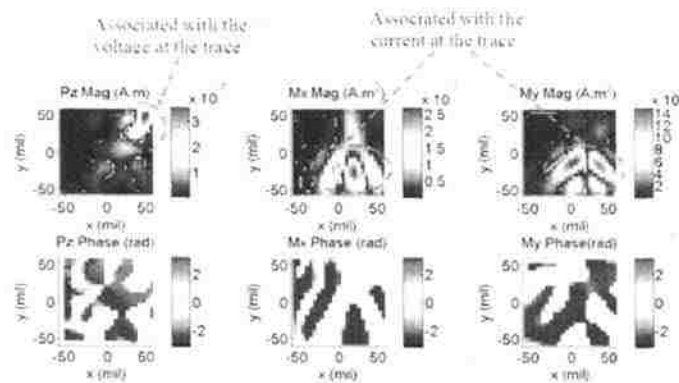
Fig. 13. The DUT and the scanned fields. (a) The top view of the DUT. (b) The magnitude and phase of electric and magnetic field measured by a near-field scanning system.

For  $M_x$  and  $M_y$  magnetic dipole plots, there are some hotspots at lower places, which is associated with the short termination at the traces (as labelled in Fig. (a) middle and right column plots). The short termination makes the trace form a loop with the ground plane, and the current loop can be represented by magnetic dipoles.

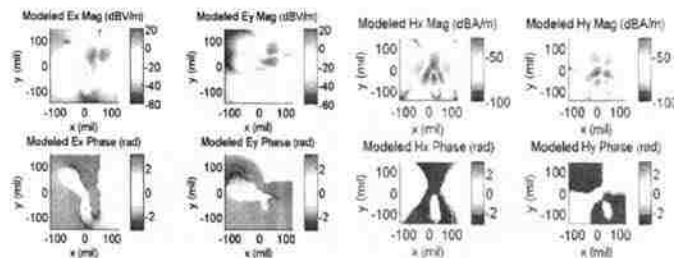
Physical dipole array are placed 5.5 mm above the ground plane. The array grid is 24 by 24, with 5 mm spacing. Using this model, the value of physical dipoles are calculated and plotted as shown in Fig. (a). For  $P_z$  electric dipole plot, there is a hotspot

at right upper corner, which is associated with the open termination at the trace over there (as labeled in Fig. (a) left column plots). The open termination makes electric charges accumulated at the trace, and causes voltage drop between the trace and the ground plane, the charges (or the voltage drop) can be represented by electric dipoles.

The electric and magnetic fields generated by physical dipoles at the scanning plane are plotted as shown in Fig. (b), and they agree well with the fields measured as shown in Fig. (b). The error of electric field and magnetic field are 16% and 14%, respectively, according to the definition in (37).



(a)



(b)

Fig. 14. Field dipoles and field generated by the dipoles. (a) Physical dipole array magnitude and phase plot, from left to right are electric dipoles Pz, magnetic dipoles Mx and magnetic dipoles My respectively. (b) The magnitude and phase of electric and magnetic field generated by physical dipoles.

## VI. CONCLUSIONS

This paper proposes an improved dipole-moment model for IC, based on near-field scanning. A set of dipole moments, which could correlate with IC voltage and current better, are carefully chosen for the problem under study. The regularization technique and the truncated SVD method are investigated to eliminate the effect of noise/error in near-field scanning. As a result, it is demonstrated that the extracted dipole moments could now reflect the actual voltage and current distributions in the IC. Consequently the improved source model is not only good at modeling far-field emissions, but also can evaluate near fields accurately, necessary for RFI investigations.

## VII. REFERENCE

- [1] M. Ramdani, E. Sicard, A. Boyer, S. Ben Dhia, J. J. Whalen, T. H. Hubing, M. Coenen and O. Wada, "The Electromagnetic Compatibility of Integrated Circuits—Past, Present, and Future," *IEEE Trans. Electromagn. Compat.*, vol. 51, no. 1, pp. 78—100, Feb. 2009.
- [2] *Integrated Circuits, Measurement of Electromagnetic Emission, 150 KHz–1 GHz: General Conditions and Definitions—Part 1*, International Electrotechnical Commission Standard IEC61967-1, Mar. 2002.
- [3] *Integrated Circuits, Measurement of Electromagnetic Immunity, 150 KHz–1 GHz: General Conditions and Definitions—Part 1*, International Electrotechnical Commission Standard IEC62132-1, 2007.
- [4] *Models of Integrated Circuits for EMI Behavioral Simulation*, International Electrotechnical Commission Standard IEC/TR 62014-3, Nov. 2004.
- [5] J. L. Levant, M. Ramdani, and R. Perdriau, "ICEM modeling of microcontroller current activity," *Microelectron. J.*, vol. 35, no. 6, pp. 501–508, Jun. 2004.



- [6] *Logic Digital Integrated Circuits—Specification for I/O Interface Model for Integrated Circuits (IMIC Version 1.3)*, International Electrotechnical Commission Standard IEC/TS 62404, 2007.
- [7] *EMC IC Modeling—Part 1: General Modeling Framework*, International Electrotechnical Commission Standard IEC62433-1, 2006.
- [8] *Models of Integrated Circuits for EMI Behavioral Simulation—Conducted Emission Modeling (ICEM-CE)*, International Electrotechnical Commission Standard IEC62433-2, 2006.
- [9] P. Petre and T. K. Sarkar, “Planar near-field to far-field transformation using an equivalent magnetic current approach,” *IEEE Trans. Antennas Propag.*, vol. 40, no. 11, pp. 1348–1355, Nov. 1992.
- [10] A. Taaghola and T. K. Sarkar, “Near-field to near/far-field transformation for arbitrary near-field geometry, utilizing an equivalent magnetic current,” *IEEE Trans. Electromagn. Compat.*, vol. 38, no. 3, pp. 536–542, Aug. 1996.
- [11] T. K. Sarkar and A. Taaghola, “Near-field to near/far-field transformation for arbitrary near-field geometry utilizing an equivalent electric current and MoM,” *IEEE Trans. Electromagn. Compat.*, vol. 47, no. 3, pp. 566–573, Mar. 1999.
- [12] H. Weng, D. G. Beetner, R. E. DuBroff, “Prediction of Radiated Emissions Using Near-Field Measurements,” *IEEE Trans. Electromagn. Compat.*, vol. 53, no. 4, pp. 891–899, Nov. 2011.
- [13] J. Shi, M. Cracraft, J. Zhang, R. DuBroff, K. Slattery, and M. Yamaguchi, “Using near-field scanning to predict radiated fields,” in *Proc. IEEE Int. Symp. Electromagn. Compat.*, Santa Clara, CA, 2004, pp. 14–18.

- [14] Y. Alvarez, M. Rodriguez, F. Las-Heras, and M. Hernando. "On the Use of the Source Reconstruction Method for Estimating Radiated EMI in Electronic Circuits." *IEEE Trans. Instrum. and Meas.* vol. 59, no. 12, pp. 3174–3183, Dec. 2010.
- [15] M. Hernando, A. Fernandez, M. Arias, M. Rodriguez, Y. Alvarez, and F. Las-Heras. "EMI Radiated Noise Measurement System Using the Source Reconstruction Technique," *IEEE Trans. Ind. Electron.*, vol. 55, no. 9, pp. 3258-3265, Sep. 2008.
- [16] Y. Vives, C. Arcambal, A. Louis, F. de Daran, P. Eudeline, and B. Mazari. "Modeling Magnetic Radiations of Electronic Circuits using Near-Field Scanning Method," *IEEE Trans. Electromagn. Compat.*, vol. 49, no. 2, pp. 391–400, May 2007.
- [17] D. Baudry, C. Arcambal, A. Louis, B. Mazari, and P. Eudeline, "Applications of the near-field techniques in EMC investigations," *IEEE Trans. Electromagn. Compat.*, vol. 49, no. 4, pp. 805–815, Nov. 2007.
- [18] Priscila Fernández-López, Christian Arcamba, David Baudry, Serge Verdeyme, Bélahcène Mazari, "Radiation Modeling and Electromagnetic Simulation of an Active Circuit", in *Proc. of the 7th Int. Workshop on Electromagnetic Compatibility of Integrated Circuits*, Toulouse, France, November. 2009.
- [19] W. He, "Characterizing near-field circuit board radiation using crossed electric and magnetic dipoles sources," M. Eng. thesis, Missouri University of Science and Technology, Rolla, MO, 2010.
- [20] P. Fernández López, C. Arcambal, S. Verdeyme, D. Baudry, and B. Mazari. "Near-field Measurements to Create a Model Suitable for a Commercial Simulation Tool" in *Proc. of the 4th Int. Conference on Electromagnetic Near-Field Characterization and Imaging*, Taipei, Taiwan, June 2009.

- [21] P. Fernández López, A. Ramanujan, Y. Vives Gilabert, C. Arcambal, A. Louis, and B. Mazari, "A Radiated Emission Model Compatible to a Commercial Electromagnetic Simulation Tool", in *Proc. 20th Int. Symp. Electromagn. Compat.*, Zurich, Switzerland, January 2009, pp. 369–372.
- [22] P. Fernández López, C. Arcambal, D. Baudry, S. Verdeyme, and B. Mazari, "Simple Electromagnetic Modeling Procedure: From Near-Field Measurements to Commercial Electromagnetic Simulation Tool", *IEEE Trans. Instrum. and Meas.* vol. 59, no. 12, Dec. 2010.
- [23] H. Fan and F. Schlagenhauer, "Near-field Far-field conversion based on genetic algorithm for predicting radiation from PCBs," in *Proc. IEEE Int. Symp. Electromagn. Compat.*, Honolulu, HI, July. 2007, pp. 1–6.
- [24] J. R. Regue, M. Ribo, J. Gomila, A. Perez, and A. Martin, "Modeling of radiating equipment by distributed dipoles using metaheuristics methods." in *Proc. IEEE Int. Symp. Electromagn. Compat.*, Chicago, IL, Aug. 2005, pp. 8–12.
- [25] Y. Vives-Gilabert, C. Arcambal, A. Louis, P. Eudeline, and B. Mazari, "Modeling magnetic emissions combining image processing and an optimization algorithm," *IEEE Trans. Electromagn. Compat.*, vol. 51, no. 4, pp. 909–918, Nov. 2009.
- [26] H. Weng, D. G. Beetner, R. E. DuBroff, J. Shi, "Estimation of current from near-field measurement," *IEEE Trans. Electromagn. Compat.*, vol. 1, pp. 222–227, Aug 2005.
- [27] R. D. Throne and L. G. Olson, "A Generalized Eigensystem Approach to the Inverse Problem of Electrocardiography", *IEEE Trans. Biomedical engineering*, vol. 41, no.6, pp. 592–600, June 1994.

- [28] R. M. Gulrajani, "The forward and inverse problems of electrocardiography." *Engineering in Medicine and Biology Magazine, IEEE*, vol. 17, pp. 84–101, Sept. 1998.
- [29] C. R. Johnson, "The Generalized Inverse Problem in electrocardiography: Theoretical, Computational, and experimental Results," Ph. D. dissertation, The University of Utah, Salt Lake City, UT, 1990.
- [30] C. R. Johnson, "The Generalized Inverse Problem in electrocardiography." In *Proc. 12th Ann. Int. Conf. IEEE Eng. Med Biol. Soc*, pp. 593–594, 1990.
- [31] P. Wilson, "On Correlating TEM Cell and OATS Emission Measurements." *IEEE Trans. Electromagn. Compat.*, vol. 37, no. 1, pp. 1–16, Feb. 1995.
- [32] C. A. Balanis, *Antenna Theory: Analysis and Design*, 3rd ed., Hoboken, New Jersey, USA: John Wiley & Sons, Inc., 2005.
- [33] HFSS 12.0 (High Frequency Structure Simulator) from ANSYS. Available: <http://www.ansys.com>.
- [34] R. Kress, *Numerical Analysis*, Springer-Verlag New York, Inc., 1998.

## II. Heat-Sink Modeling and Design with Dipole Moments

### Representing IC Excitation

Zhenwei Yu, *Student Member, IEEE*, David Pommerenke, *Senior Member, IEEE* and Jun Fan, *Senior Member, IEEE*

*Abstract*— Electromagnetic field coupling and radiation from a heat-sink is a challenging issue in the electromagnetic compatibility design of high-speed circuits. In order to accurately predict the fields excited by a heat sink, an approach is proposed in this paper to include the exact excitation of the heat sink, which is described by some dipole moments constructed from the near-field scanning of the integrated circuit beneath the heat sink. With both the dipole moments and the passive heat-sink structure incorporated in a full-wave model, near-field coupling and far-field radiation can be estimated, and the heat-sink structure can be optimized for mitigating unintentional interferences. Two examples are used to validate and demonstrate the proposed approach.

#### I. INTRODUCTION

With continuous development in integrated circuit (IC) technology, power levels of devices continuously increase, and heat sink becomes an indispensable component in IC packaging configurations. Typical heat sink is metallic and is in close proximity to an IC, an electromagnetic noise source. At the low frequencies where the electrical dimensions of a heat sink structure are much smaller than the wavelength of concern, the heat sink may not be an efficient radiator; however, it could still become a noise source for nearby victims through near-field coupling. As the frequency goes higher and the heat-sink dimensions become comparable to or larger than the wavelength, significant electromagnetic emissions could result from the heat sink. Therefore, to analyze and

mitigate interference/radiation problems from a heat sink, its structure needs to be carefully modeled and designed.

Considerable research has been conducted on the simulation and modeling of heat sinks [1]-[9]. Different models were proposed using numerical techniques such as the FDTD method [3]-[5] and the finite element method (FEM) [9]. Heat sink structure was initially modeled as a metallic box for simplicity [1], [3], and later, the more complicated fin structure was studied for more accurate results [7]-[8]. An analytical approach was also proposed to estimate the maximum radiated emissions from a heat sink [10]. Mitigation of radiation from heat sink structures was further proposed by using shorting posts, resistive loading, and absorbing material between heat sink and ground plane [3], [11].

The electromagnetic fields from a heat sink depend on both the structure of the heat sink and its excitation. Given the same heat sink structure, if the excitation location or type is different, the fields could be totally different. In conventional heat-sink modeling and mitigation studies, the most common source model to excite a heat-sink configuration is a voltage source between the heat sink and the ground plane [10]. Simple electric and magnetic dipoles with the vertical and horizontal orientations were also proposed in [3]. However, these dipole moments by no means represented the actual excitation caused by the IC.

An approach to estimate the accurate electromagnetic fields from a heat sink structure is proposed in this paper, to incorporate the exact excitation due to the IC beneath the heat sink. The IC is modeled with an array of dipole moments obtained from the near-field scanning of the IC. An improved dipole-moment model for ICs which is

particular suitable for these kinds of applications is briefly reviewed in Section II. Details of the incorporation of the improved dipole-moment model as the excitation to heat-sink structures are introduced in Section III, validated and demonstrated using two simple examples.

## II. AN IMPROVED DIPOLE-MOMENT MODEL OF IC

Many methods have been proposed to model the electromagnetic fields from an IC based on measurements like near-field scanning [12]-[21]. In heat-sink applications, the category of the models based on the Huygens' equivalence principle using the equivalent current densities in the scanning plane [12]-[15] is obviously not suitable, since the tangential fields in the scanning plane from the IC could change drastically when a heat sink is introduced. Source reconstruction models using equivalent current densities or dipole moments located at the IC [16]-[20] are more suitable in this case. However, careful considerations should be given when such a model is constructed. An improved dipole-moment model was proposed in [22], where an array of electric and magnetic dipoles with a uniform pitch size is employed to represent an IC for field estimations as shown in Fig. 1. There are three dipoles in each group:  $P_z$  (vertical electric dipole),  $M_x$  and  $M_y$  (horizontal magnetic dipoles), which were carefully chosen to represent the voltage and current distributions in the IC above a large ground plane. The values of these dipoles were determined from the near field measurements in a scanning plane above the IC. Special care was taken in the dipole moment calculations so that the effect of the ground plane was not included in the dipole moments by introducing the image dipoles [16]. This is very important for the situations such as the heat-sink applications where multiple scattering could occur.

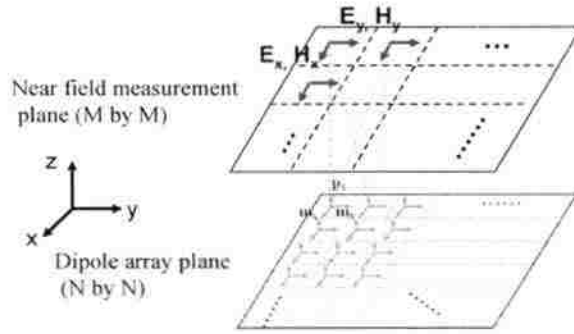


Fig. 1. Equivalent dipole-moment model for field calculations from an IC, based on near-field scanning measurements.

The fields generated by the dipole array are contributed by all the dipoles in the array, and can be calculated as

$$\begin{pmatrix} [E_x]_{M^2 \times 1} \\ [E_y]_{M^2 \times 1} \\ [H_x]_{M^2 \times 1} \\ [H_y]_{M^2 \times 1} \end{pmatrix} = T \begin{pmatrix} [P_z]_{N^2 \times 1} \\ [M_x]_{N^2 \times 1} \\ [M_y]_{N^2 \times 1} \end{pmatrix} \quad (1)$$

where  $[E_x]$ ,  $[E_y]$ ,  $[H_x]$  and  $[H_y]$  denotes the x- and y- components of the electric and magnetic fields assessed in the scanning plane; the number of the measurement points in the scanning plane is assumed to be  $M \times M$ ; vectors  $[P_z]$ ,  $[M_x]$ , and  $[M_y]$  are the electric and magnetic dipole moments in the dipole array located at the IC;  $N \times N$  groups of these dipoles are assumed; and,  $T$  is a  $4M^2 \times 3N^2$  field generation matrix whose elements can be calculated using the expressions given in [22]. Equation (1) can be rewritten as

$$F_n = T_{nk} X_k \quad (2)$$

where  $F_n$  and  $X_k$  are the normalized forms of the field and source vectors in (1). The regularization approach was then proposed in [22] to solve the inverse problem, in order



to obtain a solution that could reflect the actual voltage and current distributions in the IC. In other words, the source vector can be calculated as

$$X_k^{exc} = [T_{nk}' T_{nk} + \lambda^2]^{-1} T_{nk}' F_n \quad (3)$$

where  $T_{nk}'$  is the transpose conjugation of  $T_{nk}$ ; and,  $\lambda$  is the regularization coefficient, whose value can be selected based on the estimated error in the near-field data. It is demonstrated in [22] that having a solution reflecting the actual voltage and current distributions can ensure the accuracy in not only the far-field, but also the near-field evaluations using the equivalent source. This is particularly useful for heat-sink applications where the IC is in close proximity to the heat-sink structure. Having a reliable equivalent source ensures the correct excitation of the heat-sink structure.

### III. INCORPORATION OF IMPROVED DIPOLE-MOMENT MODEL IN HEAT-SINK MODELING

When a reliable equivalent model is established for field calculations from an IC, it can be used in heat-sink modeling and design by replacing the IC with the equivalent model. This way a realistic excitation can be applied to the heat-sink structure under study. As illustrated in Fig. 2, an IC located between a heat sink and a finite ground plane is replaced by an array of dipoles. As discussed earlier, when the dipole-moment model reflects the actual voltage and current distributions in the IC and the model itself does not include the effect of the ground plane, the heat sink can be properly excited as if the real IC is present. Furthermore, multiple scattering between the ground plane and the heat-sink can also be properly taken care of.



Fig. 2. Generating a realistic excitation for heat-sink studies using dipole moments to replace the IC underneath the heat sink.

The dipoles need to be located at the IC. More specifically, they are  $d/2$  above the ground plane where  $d$  is the distance from the IC lead frame to the ground plane [16]. When the number of the dipoles is small, it is possible to add the dipoles into a full-wave model manually. However, when the number gets large for large-sized ICs, it is preferable to incorporate these dipoles into the full-wave model automatically. Many full-wave tools can handle dipoles as sources, such as HFSS and EMC Studio. For brevity, EMC Studio is used in this paper as an example. To automatically incorporate dipoles into an EMC Studio model, a text file describing the dipole information is needed. A simple example file is shown in Fig. 3, where the magnitude, phase, type and location information is defined for each dipole. An electric dipole is type 0 while a magnetic one is type 1. The unit of an electric dipole is  $A \cdot m$ , and that of a magnetic dipole is  $A \cdot m^2$ . Since the file structure for each dipole is the same, a Matlab script can be developed to generate the text file automatically containing all of the information for the dipole array. It should be pointed out that there is a slight difference in the magnetic dipole definitions between Equation (1) in [22] and EMC Studio [23]. For a current loop as shown in Fig. 4, the magnetic dipole moment in [22] is defined as

$$M_1 = \pi a^2 I \quad (4)$$

where  $I$  is the current in the loop; and,  $a$  is the radius of the loop. However, in EMC Studio, the magnetic dipole moment is defined as

```

-----
begin excitation
begin dipole
begin dipole 1
name =
filename =
current = 0
magnitude = 2.7675e-007
phase = -155.2602
theta = 0
phi = 0
param1 = 1
param2 = 0
param3 =
param4 =
param5 =
position_x = 0.004572
position_y = 0.004572
position_z = 0
type = 0
field_type = 0
end dipole 1
-----

```

Magnitude and Phase of the dipole

x, y, z location of the dipole source in meter

Fig. 3. The text file used in EMC Studio to describe the information of a dipole.

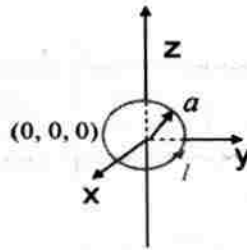


Fig. 4. A x-directional magnetic dipole: different magnetic dipole definitions.

$$M_2 = j\eta k\pi a^2 I \quad (5)$$

where  $k$  is the wave number;  $\eta$  is the wave impedance in vacuum; and,  $j$  is the imaginary number unit. In other words,

$$M_2 = j\eta k M_1 \quad (6)$$

After the dipoles are incorporated into the full-wave model of a heat-sink structure, both the near-field coupling and far-field radiation from the heat-sink structure can be accurately evaluated using full-wave simulations, with a realistic excitation. To validate and demonstrate the proposed approach, two simple examples were studied. First of all, the IC is simplified as a trace above a ground plane in vacuum, as shown in Fig. 5. The distance between the trace and the finite ground plane is 10 mils. The ground plane dimensions are 2000 mils in both the x and y directions. The width and the length of the trace are 40 mils and 1200 mils, respectively. An open patch with the sizes of 80 mils by

80 mils is connected to one end of the trace. A source with one-volt voltage and a 50-ohm impedance is added between the trace and the ground plane at the interface between the trace and the patch. The other end of the trace is terminated with a 50-ohm load.

A near-field scanning plane (800 mils by 800 mils large) is selected, which is 50 mils above the ground plane. Tangential electromagnetic fields are simulated in this plane, as shown in Fig. 5. The fields at  $40 \times 40$  observation points in the plane with a pitch size of 20 mils are calculated.

Totally  $31 \times 31$  groups of dipole moments with a pitch size of 20 mils are used as the equivalent model for the trace structure for field calculations. These dipoles are located halfway between the trace and the ground, which is 5 mils above the ground

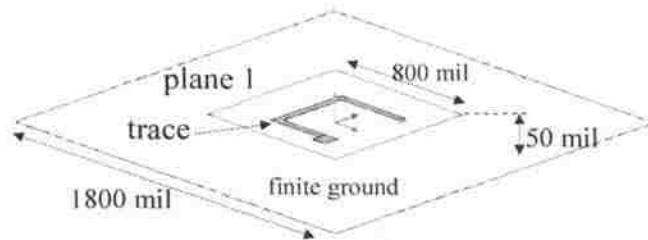


Fig. 5. An example trace structure used to mimic an IC.

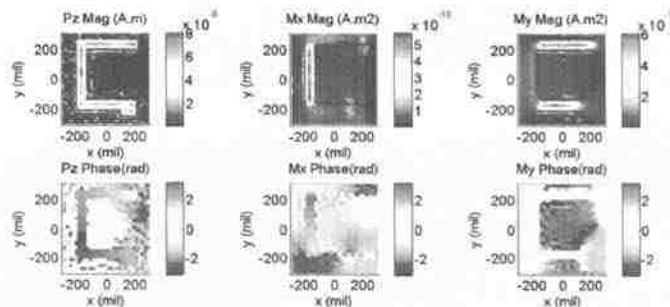


Fig. 6. The equivalent dipole moments for the trace structure shown in Fig.5, obtained using the regularization approach from near-field data.

plane. The magnitudes and phases of these dipoles are obtained from (3) and plotted in Fig. 6. It is clearly seen that these dipole moments reflect the voltage and current distributions in the trace structure, as discussed in [22].

The first heat-sink example is shown in Fig. 7(a), where a simple perfect electric conductor (PEC) box is added above the trace structure shown in Fig. 5. The box is 50 mils above the ground plane, and has dimensions of 600 mils x 600 mils x 200 mils. In Fig. 7(b), the proposed approach in this paper is applied. The trace structure is replaced with the dipole moments shown in Fig. 6 and the rest of the structure remains the same.

The electromagnetic fields in a plane 400 mils above the ground plane for both models shown in Fig. 7 (a) and (b) are calculated in EMC Studio, and are compared in Fig. 8. It can be clearly seen that the electromagnetic fields calculated from the heat-sink structure with the equivalent dipole-moment excitation agree very well with those calculated from the original structure with the real excitation. This validates the proposed approach.

The relative error in using the equivalent dipole-moment model to replace the trace structure as the excitation to the heat-sink can be defined as

$$Error_{-F} = \frac{\|F^{cal} - F^{ref}\|}{\|F^{ref}\|} \quad (7)$$

where the superscripts *ref* and *cal* denote the fields calculated from the real trace structure and from the equivalent dipole-moment model, respectively; and,

$$\|F\| = \sqrt{\sum_{i,j} [F_x(i,j)^2 + F_y(i,j)^2 + F_z(i,j)^2]} \quad (8)$$

where  $(i, j)$  is the index of a field observation location. The errors of electric and magnetic fields are 8.9% and 11.8%, respectively, using the above definition.

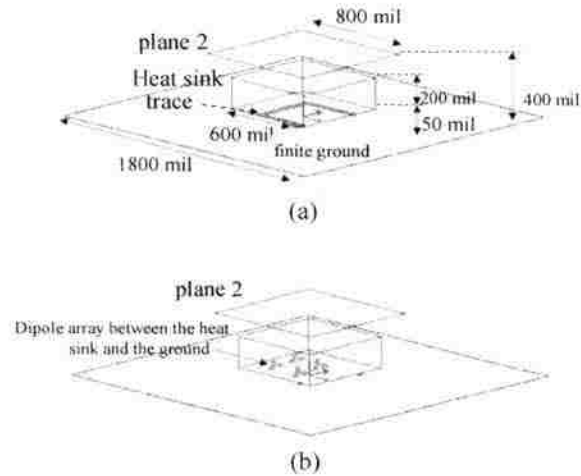


Fig. 7. The heat-sink structure simulated. (a) A simple heat-sink structure on top of the trace structure shown in Fig. 5; (b) the trace structure is replaced with the equivalent dipole-moment model shown in Fig. 6.

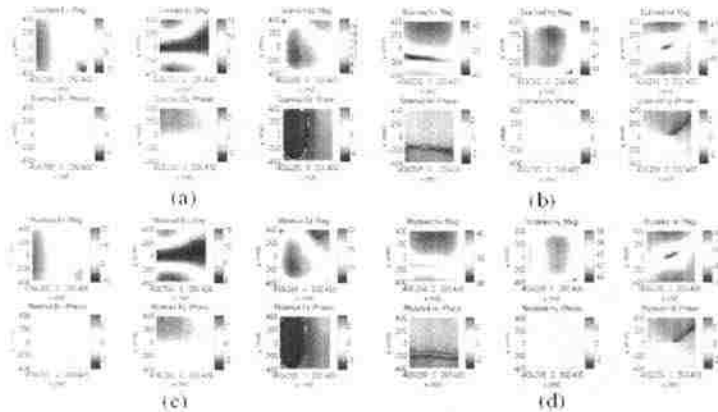


Fig. 8. Comparisons between the calculated fields from the heat-sink models in Fig. 7: (a) the electric field calculated from the equivalent dipole-moment excitation; (b) the electric field calculated from the real trace excitation; (c) the magnetic field calculated from the equivalent dipole-moment excitation; and, (d) the magnetic field calculated from the real trace excitation.

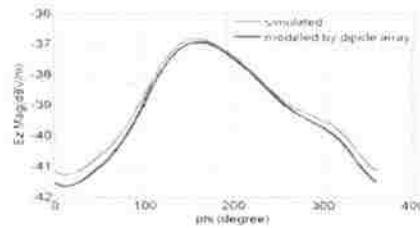


Fig. 9. Comparisons between the calculated  $E_z$  component at 3 meters away from the heat-sink models shown in Fig. 7.

The magnitudes of the electric field from the heat-sink models shown in Fig. 7 are also calculated at 3 meters away and are compared in Fig. 9, where the elevation angle  $\theta$  is 89 *degrees* and the azimuth angle  $\phi$  varies from 0 to 360 *degrees*. The results from the two models agree with each other with a difference less than 0.5 dB, again demonstrating the effectiveness of the proposed approach.

A different heat-sink structure with two PEC boxes was also studied to demonstrate the generality of the proposed approach. The heat sink is again placed 50 mils above the ground plane as shown in Fig. 10. The dimensions of each PEC box are 600 mils x 250 mils x 200 mils. And the two boxes are 100 mils apart. The same trace structure shown in Fig. 5 was used to mimic an IC, and its equivalent dipole-moment model is shown in Fig. 6. The electric and magnetic fields calculated at an observation plane 400 mils above the ground plane from the two heat-sink models shown in Fig. 10 are compared in Fig. 11. The errors of the calculated electric and magnetic fields from the equivalent dipole-moment excitation are 6.5% and 10%, respectively, based on the error definition in (7). This example indicates that more complicated heat-sink structures may be studied using the proposed approach, to investigate the electromagnetic field coupling and radiation from at sinks under realistic excitations.

It is worth mentioning here that the proposed approach has some other advantages that may be attractive for heat-sink design and optimization. The equivalent dipole-moment model of an IC in practical cases does not change significantly with or without the presence of the heat sink. Thus heat sink structures and their excitations are independent models. Typical ICs can be individually studied and their equivalent models created in a library. Then, they can be easily imported for heat-sink modeling. Parametric studies of heat-sink geometries and noise mitigation designs can be conducted to obtain the best performance in terms of minimizing the unwanted interference from heat sinks.

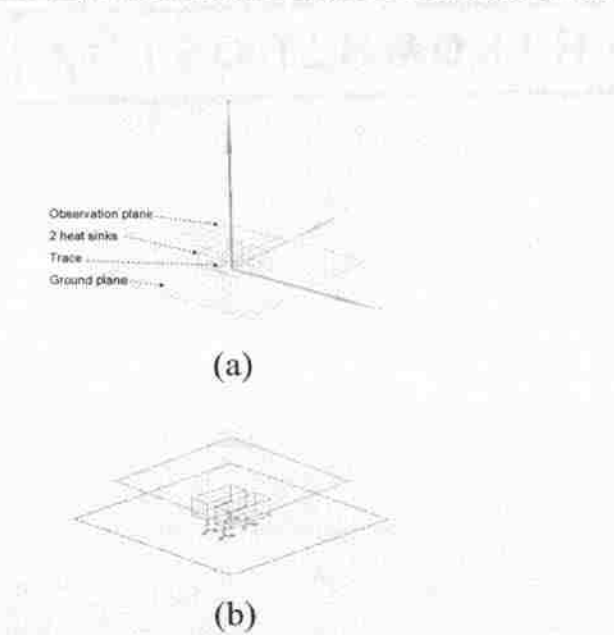


Fig. 10. Another heat-sink structure simulated. (a) Another heat-sink structure (two PEC boxes) on top of the trace structure shown in Fig. 5; (b) the trace structure is replaced with the equivalent dipole-moment model shown in Fig. 6.



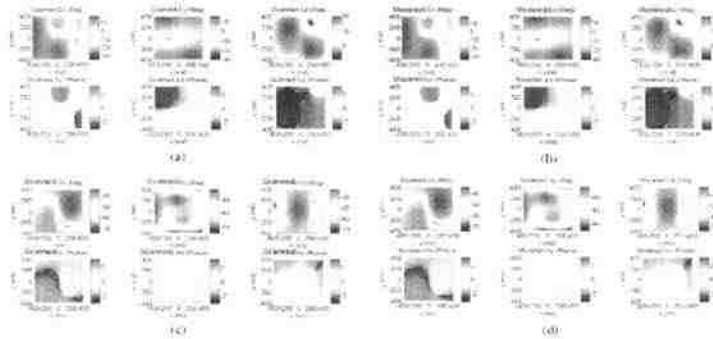


Fig. 11. Comparisons between the calculated fields from the heat-sink models in Fig. 10: (a) the electric field calculated from the equivalent dipole-moment excitation; (b) the electric field calculated from the real trace excitation; (c) the magnetic field calculated from the equivalent dipole-moment excitation; and, (d) the magnetic field calculated from the real trace excitation.

#### IV. CONCLUSIONS

In this paper, an approach is proposed to incorporate the equivalent dipole-moment model of an IC into the heat-sink model as its excitation. By using a more realistic excitation for heat-sink modeling, both the near-field coupling and the far-field radiation from the heat sink can be accurately evaluated. And, thus, meaningful optimizations of heat-sink geometries and noise mitigation designs become possible. The requirements for suitable IC models in this application are discussed, and an improved dipole-moment model based on near-field scanning is presented. The accuracy and the effectiveness of this approach are demonstrated by two simple examples.

#### V. REFERENCE

- [1] C. F. Lee, K. Li, S. Y. Poh, R. T. Shin, and J. A. Kong, "Electromagnetic radiation from a VLSI package and heatsink configuration," *Proc. 1991 IEEE Int. Symp. Electromagn. Compat.*, pp. 393–398, Aug. 1991.
- [2] C. E. Brench, "Heatsink radiation as a function of geometry," *Proc. 1994 IEEE Int. Symp. Electromagn. Compat.*, pp. 105–109, 1994.

- [3] K. Li, C. F. Lee, S. Y. Poh, R. T. Shin, J. A. Kong, "Application of FDTD method to analysis of electromagnetic radiation from VLSI heatsink configurations," *IEEE Trans. Electromagn. Compat.*, vol. 35, no. 2, pp. 204–214, 1993.
- [4] N. J. Ryan, D. A. Stone, B. Chambers, "FDTD modeling of heatsinks for EMC," *Proc. Of EMC York 99, International Conf. and Exhibition on Electromagn. Compat.*, pp. 125-130, July 1999.
- [5] N. J. Ryan, B. Chambers, and D. A. Stone, "FDTD modeling of heatsink RF characteristics for EMC mitigation," *IEEE Trans. Electromagn. Compat.*, vol. 44, no. 3, pp. 458–465, Aug. 2002.
- [6] S. K. Das and T. Roy, "An investigation of radiated emissions from heatsinks," *Proc. 1998 IEEE Symp. Electromagn. Compat.*, vol. 2, pp. 784–789, 1998.
- [7] J. Nonaka, S. Nitta, A. Mutoh, T. Miyashita, "The influence of straight-fin heatsink on noise susceptibility of IC-capacitive coupling," *Proc. 1999 IEEE Int. Symp. Electromagn. Compat.*, vol. 1, pp. 345–350, 1999.
- [8] P. Qu, M. K. Iyer, Y. Qiu, "Radiated emission from pin-fin heat sink mounted on an EPGA package," *Proc. Electrical Performance of Electronic Packaging*, pp. 199-202, 1999.
- [9] S. K. Das and T. Roy, "An investigation of radiated emissions from heatsinks," *Proc. 1998 IEEE Symp. Electromagn. Compat.*, vol. 2, pp. 784–789, 1998.
- [10] Xinbo He, "Estimating And Mitigating Radiated Emissions From Pcb Heatsinks". Ph. D Thesis.
- [11] Bruce Archambeault, Juan Chen, Satich Pratepeni, Lauren Zhang, David Wittwer, "Comparison of Various Numerical Modeling Tools Against a Standard Problem

Concerning Heat Sink Emissions - Standard Modeling Paper 3," IEEE EMC Society TC9 website, <http://www.ewh.ieee.org/cmte/tc9/>.

- [12] P. Petre and T. K. Sarkar, "Planar near-field to far-field transformation using an equivalent magnetic current approach," *IEEE Trans. Antennas Propag.*, vol. 40, no. 11, pp. 1348–1355, Nov. 1992.
- [13] A. Taaghola and T. K. Sarkar, "Near-field to near/far-field transformation for arbitrary near-field geometry utilizing an equivalent magnetic current," *IEEE Trans. Electromagn. Compat.*, vol. 38, no. 3, pp. 536–542, Aug. 1996.
- [14] T. K. Sarkar and A. Taaghola, "Near-field to near/far-field transformation for arbitrary near-field geometry utilizing an equivalent electric current and MoM," *IEEE Trans. Electromagn. Compat.*, vol. 47, no. 3, pp. 566–573, Mar. 1999.
- [15] H. Weng, D. G. Beetner, R. E. DuBroff, "Prediction of Radiated Emissions Using Near Field Measurements," submitted to *IEEE Trans. Electromagn. Compat.*
- [16] Y. Alvarez, M. Rodriguez, F. Las-Heras, and M. Hernando, "On the Use of the Source Reconstruction Method for Estimating Radiated EMI in Electronic Circuits," *IEEE Trans. Instrum. and Meas.*, vol. 59, no. 12, pp. 3174–3183, Dec. 2010.
- [17] M. Hernando, A. Fernandez, M. Arias, M. Rodriguez, Y. Alvarez, and F. Las-Heras, "EMI Radiated Noise Measurement System Using the Source Reconstruction Technique," *IEEE Trans. Ind. Electron.*, vol. 55, no. 9, pp. 3258–3265, Sep. 2008.
- [18] J. Shi, M. Cracraft, J. Zhang, R. DuBroff, K. Slattery, and M. Yamaguchi, "Using near-field scanning to predict radiated fields," in *Proc. IEEE Int. Symp. Electromagn. Compat.*, Santa Clara, CA, 2004, pp. 14–18.

- [19] Y. Vives, C. Arcambal, A. Louis, F. de Daran, P. Eudeline, and B. Mazari, "Modeling Magnetic Radiations of Electronic Circuits using Near-Field Scanning Method," *IEEE Trans. Electromagn. Compat.*, vol. 49, no. 2, pp. 391-400, May 2007.
- [20] D. Baudry, C. Arcambal, A. Louis, B. Mazari, and P. Eudeline, "Applications of the near-field techniques in EMC investigations," *IEEE Trans. Electromagn. Compat.*, vol. 49, no. 4, pp. 805-815, Nov. 2007.
- [21] S. Pan, J. Kim, S. Kim, J. Park, H. Oh, J. Fan, "An Equivalent Three-Dipole Model for IC Radiated Emissions Based on TEM Cell Measurements," *Proc. 2010 IEEE Int. Symp. Electromagn. Compat.*, pp. 652-656, July, 2010.
- [22] Z. Yu and J. Fan, "An Improved Dipole-Moment Model Based on Near-Field Scanning for Characterizing Near-Field Coupling and Far-Field Radiation from an IC," submitted to *IEEE Trans. Electromagn. Compat.*.
- [23] EMC Studio 6.0 from EMCoS. Available: <http://www.emcos.com>.

### III. An Effective Dielectric Property of Layered Media for Cavity Model

#### Applications

Zhenwei Yu, Student Member, IEEE, and Jun Fan, Senior Member, IEEE

*Abstract*—The work proposes an effective dielectric property of layered media for cavity model applications. With the effective property, the cavity model can be generalized to parallel plates or metal enclosures containing multiple dielectric layers. Simulations validated the effective property for both parallel plates and metal enclosures.

#### I. INTRODUCTION

Simultaneous switching noise (SSN) is a critical problem in high-speed packages and printed circuit boards (PCBs) [1]. It can easily propagate in power/ground plane pairs, resulting in various signal integrity and electromagnetic interference issues. Full-wave numerical techniques, such as the finite element method (FEM) and the finite difference time domain method (FDTD) are too time-consuming to study this noise coupling problem. Therefore, the work in [2] takes advantage of the fast simulation speed of the cavity model for PCB plane-pair and enclosure modelling. The cavity model provides a fast analytical solution to microwave planar circuit problems for simple shapes like rectangles or isosceles triangles [2], [3]. It is widely used in noise coupling analysis in high speed packages [4] and printed circuit boards [5]-[7]. The employment of the segmentation method [8]-[11] permits extension of the analysis to an irregularly shaped plane pair. Another scenario in which the cavity model is appropriate is a shielding metallic enclosure containing a PCB [12].

Although the cavity model is very efficient in noise coupling in parallel plate structures, previous work has applied it to one-layer media only. The current cavity model is inapplicable in cases involving two or more layers. No single uniform dielectric property has been identified for use in analytical equations in the cavity model. With the development of PCB technology, multilayer dielectric media has come to be used more frequently in power/ground plane design as shown in Fig. 1(a). On the other side, metallic enclosures also contain both dielectric and air layers in many cases. Therefore, an effective dielectric property is needed to apply the cavity model to multilayer dielectric structures.

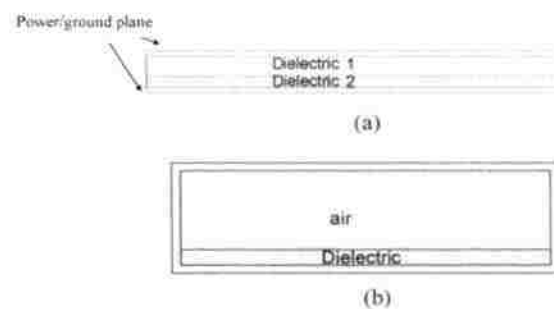


Fig. 1. Structures with dielectric layers: (a) a multilayer dielectric PCB structure; (b) a metallic enclosure with both dielectric and air layers.

Hasegawa et al.[13] have published work on an effective dielectric property for a microstrip containing two-layer dielectric material. The equation calculates effective dielectric property for a two-layer case, and can be generalized to a case with three or more layers if those layers are thin. The present work proposes an effective dielectric property in the application of the cavity model. It develops an equation that can be solved for a property applicable in either a PCB or a metallic enclosure. The effective dielectric property, or the effective complex permittivity, can be found numerically, and when each layer is thin it has an analytical solution.

The rest of the paper is organized as follows. Part II reviews a cavity model. Part III derives the equation for the effective dielectric property in a two-layer case and generalizes it to a three-layer case. It also discusses the approximate solution to the equation when all layers are thin. Part IV offers three examples for validation. One is a parallel metallic plate-pair containing three thin dielectric layers simulated in a full-wave simulation tool. Another example validated by simulation is a metallic enclosure with three dielectric layers, and the layers are not so thin. Conclusions are made in Part VI.

## II. CAVITY MODEL

This section uses the cavity model to obtain the network parameters of a parallel plane pair, as shown in Fig. 2. Two rectangular perfect electric condition (PEC) planes form a cavity. The x- and y-dimension of the rectangular plane are  $a$  and  $b$ , and the spacing between the two planes is  $d$ , which is much less than the wavelength  $\lambda$ . The dielectric material has a relative permittivity of  $\epsilon_r$  and a loss tangent of  $\tan \delta$ . At the edge of the planes are perfect magnetic condition (PMC) walls. Ports  $i$  and  $j$  are two ports defined between the two planes, and their x- and y-dimensions are  $L_{x_i}, L_{y_i}, L_{x_j}$ , and  $L_{y_j}$ , respectively. A uniformly distributed impressed current density  $J_z$  is assumed to be located at port  $i$ :

$$J_z = \begin{cases} \frac{I_i}{L_{x_i} L_{y_i}}, & \text{inside port } i \\ 0, & \text{outside port } i \end{cases} \quad (1)$$

The average voltage at port  $j$  is then defined as

$$V_j = \frac{1}{L_{x_j} L_{y_j}} \int_{L_{x_j}} \int_{L_{y_j}} v(x, y) dx dy. \quad (2)$$

The transfer impedance can be calculated as

$$Z_{ji} = \frac{V_j}{I_i} \Bigg|_{I_k=0, \text{ for } k \neq i} \quad (3)$$

Therefore, the problem is to solve for the field distribution inside the cavity under impressed current  $J_z$ .

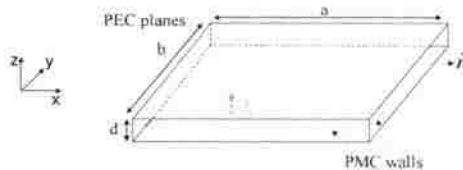


Fig. 2. A parallel plane pair excited by impressed current.

The Maxwell Equation inside the cavity can be written as [2]

$$\nabla \times \vec{E} = -j\omega\mu\vec{H} \quad (4)$$

and

$$\nabla \times \vec{H} = \vec{J} + j\omega\varepsilon\vec{E}. \quad (5)$$

Based on (4) and consider the transverse components only, it can be written as

$$\left( \frac{\partial E_z}{\partial y} - \frac{\partial E_y}{\partial z} \right) \hat{x} - \left( \frac{\partial E_z}{\partial x} - \frac{\partial E_x}{\partial z} \right) \hat{y} = -j\omega\mu\vec{H}_t. \quad (6)$$

Equation (6) can then be multiplied by the unit vector in z direction  $\hat{z}$

$$\left( \frac{\partial E_z}{\partial y} - \frac{\partial E_y}{\partial z} \right) \hat{y} + \left( \frac{\partial E_z}{\partial x} - \frac{\partial E_x}{\partial z} \right) \hat{x} = -j\omega\mu\hat{z} \times \vec{H}_t. \quad (7)$$

Due to planarity,  $\frac{\partial}{\partial z} = 0$ , and (7) becomes

$$\nabla_t E_z = -j\omega\mu\hat{z} \times \vec{H}_t \quad (8)$$

where



$$\nabla_t \equiv \frac{\partial}{\partial x} \hat{x} + \frac{\partial}{\partial y} \hat{y}. \quad (9)$$

Consider only the longitude component in

(5), that component becomes

$$\nabla_t \times \vec{H}_t = (j\omega\epsilon E_z + J_z) \hat{z}. \quad (10)$$

Due to planarity, only the  $TM_{z0}$  mode exists in the cavity, which means the E-field has only z-component, and H-field has only x- and y-components. The voltage at each point of the planar circuit is

$$v(\vec{r}) = -hE_z, \quad (11)$$

and the surface current is

$$J_s(\vec{r}) = -\hat{z} \times \vec{H}_t. \quad (12)$$

If (11) and (12) are substituted into (8) and (10), respectively, they can be written as

$$\nabla_t v = -j\omega\mu h \vec{J}_s, \quad (13)$$

and

$$\nabla_t \cdot \vec{J}_s = -j \frac{\omega\epsilon}{h} v + J_z. \quad (14)$$

The wave equation involving voltage  $v$  is then

$$\nabla_t^2 v + k^2 v = -j\omega\mu h J_z \quad (15)$$

where

$$k^2 = \omega^2 \mu \epsilon. \quad (16)$$

And the boundary condition is

$$\frac{\partial v}{\partial n} = 0. \quad (17)$$

To solve the equations (15) and (17), the Green's function  $G(x, y | x_0, y_0)$  is introduced, and it satisfies

$$\nabla_t^2 G + k^2 G = \delta(x - x_0)\delta(y - y_0), \quad (18)$$

and the boundary condition

$$\frac{\partial G}{\partial n} = 0. \quad (19)$$

For a rectangle as shown in Fig. 2, Green's function is given by

$$G(x, y | x_0, y_0) = j\omega\mu d \frac{4}{ab} \sum_n \sum_m \frac{\cos(k_{xm}x_0)\cos(k_{ym}y_0)}{k_{xm}^2 + k_{ym}^2 - k^2} \cdot \cos(k_{xm}x)\cos(k_{ym}y) \quad (20)$$

where

$$k_x = \frac{m\pi}{a}, k_y = \frac{n\pi}{b}, k = \omega\sqrt{\mu_0\epsilon_0\epsilon_r}. \quad (21)$$

The transfer impedance from port  $i$  to port  $j$  can be calculated as

$$z_{\mu} = \frac{1}{L_{x_i}L_{y_i}L_{x_j}L_{y_j}} \int_{L_{x_i}} dy \int_{L_{y_i}} dx \int_{L_{x_j}} dy' \int_{L_{y_j}} dx' G(x, y, x', y'). \quad (22)$$

Equations (20) and (22) can then be written as

$$z_{\mu} = \sum_{m=0}^{\infty} \sum_{n=0}^{\infty} \left( \frac{j\omega\mu d C_m^2 C_n^2}{P_x P_y (k_{xm}^2 + k_{ym}^2 - k^2)} \cos(k_{ym}T_{y_i}) \cos(k_{xm}T_{x_i}) \cos(k_{ym}T_{y_j}) \cos(k_{xm}T_{x_j}) \cdot \left[ \frac{\sin(k_{ym} \frac{L_{y_i}}{2})}{k_{ym} \frac{L_{y_i}}{2}} \right] \left[ \frac{\sin(k_{xm} \frac{L_{x_i}}{2})}{k_{xm} \frac{L_{x_i}}{2}} \right] \left[ \frac{\sin(k_{ym} \frac{L_{y_j}}{2})}{k_{ym} \frac{L_{y_j}}{2}} \right] \left[ \frac{\sin(k_{xm} \frac{L_{x_j}}{2})}{k_{xm} \frac{L_{x_j}}{2}} \right] \right) \quad (23)$$

where  $T_{x_1}, T_{y_1}, T_{x_2}$ , and  $T_{y_2}$  are the coordinates of the center location;  $k_{x_m}$  and  $k_{y_m}$  are defined in

(21);  $C'_m$  and  $C''_m$  are defined as

$$C'_m = \begin{cases} 1, & m = 0 \\ \sqrt{2}, & m \neq 0 \end{cases} \quad (24)$$

and

$$C''_n = \begin{cases} 1, & n = 0 \\ \sqrt{2}, & n \neq 0 \end{cases} \quad (25)$$

### III. THE EFFECTIVE DIELECTRIC PROPERTY OF THE CAVITY MODEL

#### A. Two-layer media

The effective dielectric property of layered media can be used for the cavity model for either a PCB or a metallic enclosure. For simplicity a two-layer medium problem is addressed here first. Fig. 3 shows a structure with two layers of dielectric material. The dielectric constants for each layer are  $\epsilon_1$  and  $\epsilon_2$ , and the heights are  $h_1$  and  $h_2$ . The top and bottom are PEC planes, and the four side walls are all PMC.

Since all media are uniform along z-direction, only  $TM_z$  mode waves are assumed to propagate in the media. The tangential E- and H-fields continuity at the interface between two layers can be written as

$$E_x^{up} = E_x^{down}, \quad (26)$$

and

$$H_y^{up} = H_y^{down}. \quad (27)$$

The impedance seen looking up and down at the interface can be defined as

$$Z_{up} \equiv \frac{E_x^{up}}{H_y^{up}}, \quad (28)$$

and

$$Z_{down} \equiv -\frac{E_x^{down}}{H_y^{down}}. \quad (29)$$

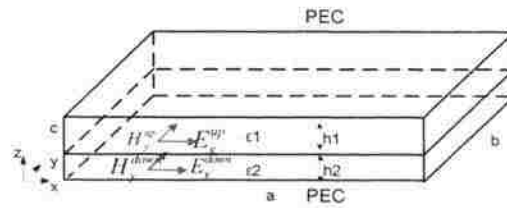


Fig. 3. A structure with a layered medium

Equations (26) and (27) can then be substituted into (28) and (29):

$$Z_{up} + Z_{down} = 0. \quad (30)$$

Then  $Z_{up}$  and  $Z_{down}$  can be calculated. Fig. 4 shows the upper layer structure, where  $Z_{up}$  is the input impedance seen looking up at  $z = -h$ , as defined in (28). Assuming only  $TM_z$  mode as before,  $TM_z$  waves may propagate in the positive or negative  $z$  ( $z^+$  or  $z^-$ ) directions. The wave impedance of the  $TM_z$  wave in the upper layer can be defined as

$$\eta_{1,TM} = \frac{E_x^+}{H_y^+} = \frac{E_y^+}{-H_x^+} = -\frac{E_x^-}{H_y^-} = \frac{E_y^-}{H_x^-} = \frac{k_{1z}}{\omega\epsilon_1} \quad (31)$$

where  $E_x^+$  and  $E_x^-$  are the x components of the electric field propagating in  $z^+$  and  $z^-$  directions;  $E_y^+$  and  $E_y^-$  are the y components;  $H_x^+$ ,  $H_x^-$ ,  $H_y^+$ , and  $H_y^-$  are components of

the magnetic field. The term  $k_{1z}$  is the propagation constant in the  $z$ -direction in the upper layer, and it is defined as

$$k_{1z} = \sqrt{k_1^2 - k_t^2} = \sqrt{\omega^2 \mu \epsilon_1 - k_t^2} \quad (32)$$

where the convention of  $\sqrt{-1} \equiv j$  is used. The term  $\omega$  is the angular frequency of the  $\text{TM}_z$  wave, and  $k_t$  is the transverse propagation constant. Equation (28) can then be written as

$$Z_{up}(-h_1) \equiv \frac{E_x(-h_1)}{H_y(-h_1)} \quad (33)$$

where  $E_x(-h_1)$  is the superposition of the waves in the  $z^+$  and  $z^-$  directions

$$E_x(-h_1) = E_x^+(-h_1) + E_x^-(-h_1). \quad (34)$$

Similarly  $H_y(-h_1)$  can be written as

$$H_y(-h_1) = H_y^+(-h_1) + H_y^-(-h_1). \quad (35)$$

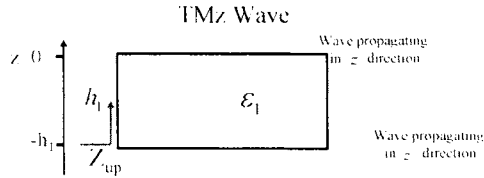


Fig. 4. The input impedance seen looking up at the interface.

By substituting (33) and (34), Equation (35) can be written as

$$Z_{up}(-h_1) = \frac{E_x^+(-h_1) + E_x^-(-h_1)}{H_y^+(-h_1) + H_y^-(-h_1)}. \quad (36)$$

It is worthwhile to notice that time-harmonic fields are assumed to have the  $e^{j\omega t}$  dependence, i. e., the term  $e^{j(\omega t - k_z z)}$  denotes wave propagating in  $z^+$  direction.  $E_x^+(-h_1)$  and  $H_y^+(-h_1)$  can be written as

$$E_x^+(-h_1) = E_x^+(0)e^{jk_z h_1} \quad (37)$$

and

$$H_y^+(-h_1) = H_y^+(0)e^{jk_z h_1} . \quad (38)$$

The terms  $E_x^-(-h_1)$  and  $H_y^-(-h_1)$  can be written as

$$E_x^-(-h_1) = E_x^-(0)e^{-jk_z h_1} , \quad (39)$$

and

$$H_y^-(-h_1) = H_y^-(0)e^{-jk_z h_1} . \quad (40)$$

Equations (37), (38), (39), and (40) can then be substituted into (36):

$$Z_{up}(-h_1) = \frac{E_x^+(0)e^{jk_z h_1} + E_x^-(0)e^{-jk_z h_1}}{H_y^+(0)e^{jk_z h_1} + H_y^-(0)e^{-jk_z h_1}} . \quad (41)$$

The PEC boundary at  $z=0$  plane can be written as

$$E_x^-(0) = -E_x^+(0) , \quad (42)$$

and

$$H_y^-(0) = H_y^+(0) . \quad (43)$$

By substituting (42) and (43) into (41), it can be written as

$$\begin{aligned} Z_{up}(-h_1) &= \frac{E_x^+(0)e^{jk_z h_1} - E_x^+(0)e^{-jk_z h_1}}{H_y^+(0)e^{jk_z h_1} + H_y^+(0)e^{-jk_z h_1}} \\ &= \frac{E_x^+(0)}{H_y^+(0)} \cdot \frac{e^{jk_z h_1} - e^{-jk_z h_1}}{e^{jk_z h_1} + e^{-jk_z h_1}} \\ &= \eta_{1,IM} \frac{2j \sin(k_z h_1)}{2 \cos(k_z h_1)} \\ &= \eta_{1,IM} j \tan(k_z h_1) \end{aligned} \quad (44)$$

where  $\tan x$ ,  $\sin x$ , and  $\cos x$  are defined as

$$\tan x \equiv \frac{\sin x}{\cos x}, \quad (45)$$

and

$$\sin x \equiv \frac{e^{jx} - e^{-jx}}{2j}, \quad (46)$$

and

$$\cos x \equiv \frac{e^{jx} + e^{-jx}}{2}. \quad (47)$$

where  $x$  can be any complex number.

Similarly, for the lower layer, the input impedance seen looking down at the interface can be calculated as

$$Z_{down}(-h_1) = \eta_{2,IM} j \tan(k_z h_2). \quad (48)$$

By substituting (32), (44), and (48) into (30), it can be written as

$$\frac{k_{2z}}{\omega \epsilon_2} \tan(k_{2z} h_2) + \frac{k_{1z}}{\omega \epsilon_1} \tan(k_{1z} h_1) = 0. \quad (49)$$

As shown in Fig. 5, the objective is to find a uniform effective dielectric property  $\epsilon_{eff}$  to replace the two-layer dielectric material. Therefore, the structure with the uniform dielectric property should have the same transverse (x-y direction) field distribution as the two-layer structure. According to the cavity model of a uniform dielectric structure, when the thickness of the cavity is electrically small, i. e., when

$$h_1 + h_2 \ll \lambda \quad (50)$$

where  $\lambda$  is the wavelength in the uniform medium, only  $TM_{z0}$  mode exists within the cavity. When resonance occurs inside the cavity, the following equation holds:

$$\omega\sqrt{\mu\epsilon_{eff}} = k = k_t \quad (51)$$

where  $k_t$  is the transverse wave number. For each layer in the two-layer structure, the following equations hold:

$$k_{1z} = \sqrt{\omega^2\mu\epsilon_1 - k_t^2}, \quad (52)$$

and

$$k_{2z} = \sqrt{\omega^2\mu\epsilon_2 - k_t^2} \quad (53)$$

where  $k_t$  is the transverse wave number. The same  $k_t$  is used in (51), (52), and (53), since both layers have the same transverse field distribution as the field in the uniform medium structure.

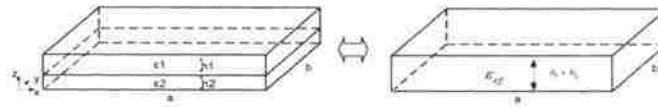


Fig. 5. Effective dielectric property  $\epsilon_{eff}$  for layered media.

Substituting (51) into (52) and (53) yields

$$k_{1z} = \sqrt{\omega^2\mu(\epsilon_1 - \epsilon_{eff})}, \quad (54)$$

and

$$k_{2z} = \sqrt{\omega^2\mu(\epsilon_2 - \epsilon_{eff})}. \quad (55)$$

Substituting (54) and

(55) into (49) yields the equation about effective dielectric property:

$$\frac{\sqrt{\epsilon_1 - \epsilon_{eff}}}{\epsilon_1} \tan(\omega h_1 \sqrt{\mu(\epsilon_1 - \epsilon_{eff})}) + \frac{\sqrt{\epsilon_2 - \epsilon_{eff}}}{\epsilon_2} \tan(\omega h_2 \sqrt{\mu(\epsilon_2 - \epsilon_{eff})}) = 0. \quad (56)$$



The equation can be solved numerically. The term  $\varepsilon_{eff}$  is a frequency dependent complex value and can be written as

$$\varepsilon_{eff} = \varepsilon_0 \varepsilon_{r,eff} (1 - j \tan \delta) \quad (57)$$

where  $\varepsilon_{r,eff}$  is the relative effective permittivity, and  $\tan \delta$  is the loss tangent. When  $h_1$  and  $h_2$  are very small (i.e., when the terms  $\omega h_1 \sqrt{\mu(\varepsilon_1 - \varepsilon_{eff})}$  and  $\omega h_2 \sqrt{\mu(\varepsilon_2 - \varepsilon_{eff})}$  are very small), the following will hold:

$$\tan(\omega h_1 \sqrt{\mu(\varepsilon_1 - \varepsilon_{eff})}) \approx \omega h_1 \sqrt{\mu(\varepsilon_1 - \varepsilon_{eff})}, \quad (58)$$

and

$$\tan(\omega h_2 \sqrt{\mu(\varepsilon_2 - \varepsilon_{eff})}) \approx \omega h_2 \sqrt{\mu(\varepsilon_2 - \varepsilon_{eff})}. \quad (59)$$

Equation (56) can then be written as

$$\varepsilon_{eff} = \frac{h}{\frac{h_1}{\varepsilon_{r1}} + \frac{h_2}{\varepsilon_{r2}}}. \quad (60)$$

By substituting (57) into (60), the effective relative permittivity and loss tangent can be written as

$$\varepsilon_{r,eff} = \frac{h}{\frac{h_1}{\varepsilon_{r1}} + \frac{h_2}{\varepsilon_{r2}}} \quad (61)$$

and

$$\tan \delta_{d,eff} = \left( \frac{h_1}{h \varepsilon_{r1}} \tan \delta_1 + \frac{h_2}{h \varepsilon_{r2}} \tan \delta_2 \right) \varepsilon_{r,eff}. \quad (62)$$

### B. Multilayered media

Equation (61) and (62) can be generalized to multilayered media. As shown in Fig.

6, the input impedance seen looking up at  $z = -h_1 - h_2$  can be written as

$$\begin{aligned}
 Z_{up}(-h_1 - h_2) &= \frac{E_x(-h_1 - h_2)}{H_y(-h_1 - h_2)} \\
 &= \frac{E_x^+(-h_1 - h_2) + E_x^-(-h_1 - h_2)}{H_y^+(-h_1 - h_2) + H_y^-(-h_1 - h_2)} \\
 &= \frac{E_x^+(-h_1)e^{jk_{z2}h_2} + E_x^-(-h_1)e^{-jk_{z2}h_2}}{H_y^+(-h_1)e^{jk_{z2}h_2} + H_y^-(-h_1)e^{-jk_{z2}h_2}} \\
 &= \frac{(E_x^+(-h_1) + E_x^-(-h_1))\cos(k_{z2}h_2) + j(E_x^+(-h_1) - E_x^-(-h_1))\sin(k_{z2}h_2)}{(H_y^+(-h_1) + H_y^-(-h_1))\cos(k_{z2}h_2) + j(H_y^+(-h_1) - H_y^-(-h_1))\sin(k_{z2}h_2)}
 \end{aligned} \tag{63}$$

Dividing the denominator and the numerator by  $(H_y^+(-h_1) + H_y^-(-h_1))\cos(k_{z2}h_2)$

simultaneously yields:

$$Z_{up}(-h_1 - h_2) = \frac{\frac{E_x^+(-h_1)}{H_y^+(-h_1)} + j \frac{(E_x^+(-h_1) - E_x^-(-h_1))}{(H_y^+(-h_1) + H_y^-(-h_1))} \tan(k_{z2}h_2)}{1 + j \frac{(H_y^+(-h_1) - H_y^-(-h_1))}{(H_y^+(-h_1) + H_y^-(-h_1))} \tan(k_{z2}h_2)}. \tag{64}$$

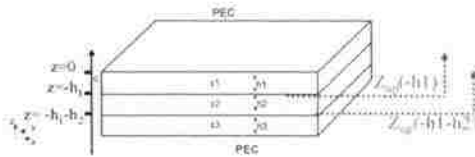


Fig. 6. The effective dielectric property  $\epsilon_{eff}$  for a three-layer medium.

The term  $\frac{E_x^+(-h_1)}{H_y^+(-h_1)}$  then becomes  $Z_{up}(-h_1)$ . Due to

$$\frac{E_x^+(-h_1)}{H_y^+(-h_1)} = -\frac{E_x^-(-h_1)}{H_y^-(-h_1)} = \eta_{2,TM}, \tag{65}$$

the following equation holds

$$\frac{(E_x^+(-h_1) - E_x^-(-h_1))}{(H_y^+(-h_1) + H_y^-(-h_1))} = \eta_{2,IM}. \quad (66)$$

Substituting (65) and (65) into (64) yields

$$Z_{up}(-h_1 - h_2) = \frac{Z_{up}(-h_1) + j\eta_{2,IM} \tan(k_{z2}h_2)}{1 + j \frac{(H_y^+(-h_1) - H_y^-(-h_1))}{(H_y^+(-h_1) + H_y^-(-h_1))} \tan(k_{z2}h_2)}. \quad (67)$$

The denominator and the numerator are multiplied by  $\eta_{2,IM}$  at the same time, (67) can be written as

$$Z_{up}(-h_1 - h_2) = \eta_{2,IM} \frac{Z_{up}(-h_1) + j\eta_{2,IM} \tan(k_{z2}h_2)}{\eta_{2,IM} + j\eta_{2,IM} \frac{(H_y^+(-h_1) - H_y^-(-h_1))}{(H_y^+(-h_1) + H_y^-(-h_1))} \tan(k_{z2}h_2)}. \quad (68)$$

Due to

$$\eta_{2,IM} = \frac{(E_x^+(-h_1) + E_x^-(-h_1))}{(H_y^+(-h_1) - H_y^-(-h_1))}, \quad (69)$$

(68) becomes

$$Z_{up}(-h_1 - h_2) = \eta_{2,IM} \frac{Z_{up}(-h_1) + j\eta_{2,IM} \tan(k_{z2}h_2)}{\eta_{2,IM} + jZ_{up}(-h_1) \tan(k_{z2}h_2)}. \quad (70)$$

Similar to the (30) in the two-layer medium case, the equation holds for the three-layer case

$$Z_{down}(-h_1 - h_2) + Z_{up}(-h_1 - h_2) = 0. \quad (71)$$

and similar equation to (56) can be found as:

$$\frac{k_{z3}}{\varepsilon_3} \tan(k_{z3}h_3) + \frac{k_{z2}}{\varepsilon_2} \frac{k_{z1} \tan(k_{z1}h_1) + \frac{k_{z2}}{\varepsilon_2} \tan(k_{z2}h_2)}{k_{z2} - \frac{k_{z1}}{\varepsilon_1} \tan(k_{z1}h_1) \tan(k_{z2}h_2)} = 0 \quad (72)$$

where  $k_{z1}$ ,  $k_{z2}$ , and  $k_{z3}$  are propagation constants in z-direction in three layers, and can be written as

$$k_{z1} = \sqrt{\omega^2 \mu (\epsilon_1 - \epsilon_{eff})}, \quad (73)$$

$$k_{z2} = \sqrt{\omega^2 \mu (\epsilon_2 - \epsilon_{eff})}, \quad (74)$$

and

$$k_{z3} = \sqrt{\omega^2 \mu (\epsilon_3 - \epsilon_{eff})}. \quad (75)$$

Like (56), (72) can be solved numerically, and  $\epsilon_{eff}$  can be calculated.

When  $h_1$ ,  $h_2$ , and  $h_3$  are very small, as is equations (58)-

(62) for the two-layer case, the effective relative permittivity and loss tangent can be written as

$$\epsilon_{r,eff} = \frac{h}{\frac{h_1}{\epsilon_{r1}} + \frac{h_2}{\epsilon_{r2}} + \frac{h_3}{\epsilon_{r3}}} \quad (76)$$

and

$$\tan \delta_{d,eff} = \left( \frac{h_1}{h \epsilon_{r1}} \tan \delta_1 + \frac{h_2}{h \epsilon_{r2}} \tan \delta_2 + \frac{h_3}{h \epsilon_{r3}} \tan \delta_3 \right) \epsilon_{r,eff}. \quad (77)$$

In the derivation of (76) and (77), the following approximation is used

$$\left[ \begin{array}{l} \tan(\omega h_1 \sqrt{\mu (\epsilon_1 - \epsilon_{eff})}) \ll 1, \\ \tan(\omega h_2 \sqrt{\mu (\epsilon_2 - \epsilon_{eff})}) \ll 1 \\ 1 - \frac{k_{z1} \epsilon_2}{k_{z2} \epsilon_1} \tan(\omega h_1 \sqrt{\mu (\epsilon_1 - \epsilon_{eff})}) \tan(\omega h_2 \sqrt{\mu (\epsilon_2 - \epsilon_{eff})}) \approx 1 \end{array} \right]. \quad (78)$$

### C. Validations

The example of a rectangular PCB with three layers of dielectric material is validated here. The x- and y-dimensions are 5 cm and 10 cm, respectively. The three dielectric layers are 2 mil, 3 mil, and 5 mil thick, respectively. The relative permittivities of the three layers are  $\epsilon_{r1} = 1$ ,  $\epsilon_{r2} = 2.3$ , and  $\epsilon_{r3} = 4.4$ , and the loss tangents of the three layers are  $\tan \delta_1 = 0.01$ ,  $\tan \delta_2 = 0.015$ , and  $\tan \delta_3 = 0.02$ , respectively. The top and bottom planes are copper layers 1 mil thick, and the conductivity is  $\sigma = 5.8 \times 10^7$  S/m. The effective dielectric property can be calculated from (76) and (77) as

$$\epsilon_{r,eff} = \frac{h}{\frac{h_1}{\epsilon_{r1}} + \frac{h_2}{\epsilon_{r2}} + \frac{h_3}{\epsilon_{r3}}} = 2.25, \quad (79)$$

and

$$\tan \delta_{d,eff} = \left( \frac{h_1}{h\epsilon_{r1}} \tan \delta_1 + \frac{h_2}{h\epsilon_{r2}} \tan \delta_2 + \frac{h_3}{h\epsilon_{r3}} \tan \delta_3 \right) \epsilon_{r,eff} = 0.014. \quad (80)$$

The two ports are placed between two copper planes, and their x- and y-coordinates are (-1.5 cm, -3 cm) and (0.5 cm, 3.5 cm), respectively. Using the effective dielectric property proposed in this paper, the transfer impedance between ports 1 and 2 is calculated by the cavity model and shown in Fig. 8. It is then compared with the result calculated using a full-wave simulation tool.

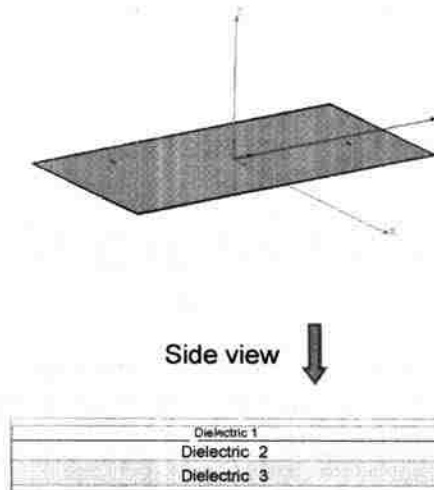


Fig. 7. A PCB with three-layer media.

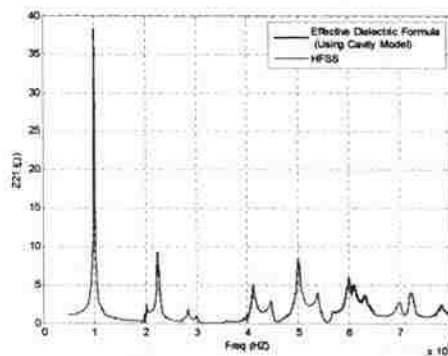


Fig. 8. The transfer impedance calculated using the effective dielectric property and the result from a full-wave simulation tool.

Another example is a metallic enclosure with the dimensions of 5 cm, 10 cm, and 1 cm in x-, y- and z-directions, respectively. All six walls of the enclosure are metal; they are 0.1 mil thick, with a conductivity of  $\sigma = 5.8 \times 10^7$  S/m. The three dielectric layers are 0.2 cm, 0.3 cm, and 0.5 cm thick, respectively. The relative permittivities of three layers are  $\epsilon_{r1} = 1$ ,  $\epsilon_{r2} = 2.3$ , and  $\epsilon_{r3} = 4.4$ , respectively, and the loss tangents of three layers are  $\tan \delta_1 = 0.01$ ,  $\tan \delta_2 = 0.015$ , and  $\tan \delta_3 = 0.02$ , respectively. The effective

dielectric property can be calculated by solving equation (72) numerically; the result is shown in Fig. 10.

The two ports are placed between the two copper planes, and their x- and y-coordinates are (-1.5 cm, -3 cm) and (0.5 cm, 3.5 cm), and the size of the ports are all 1 mm in both x- and y-directions. Using the effective dielectric property proposed in this paper, the transfer impedance between ports 1 and 2 is calculated by the cavity model (as shown in Fig. 11), and compared with the result obtained using a full-wave simulation tool.

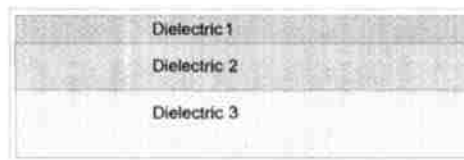


Fig. 9. A metallic enclosure with three layers of dielectric.

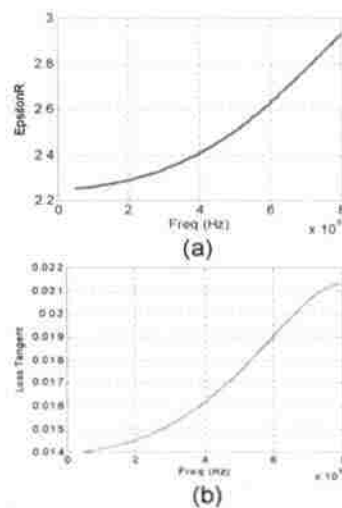


Fig. 10. The effective dielectric property of a metallic enclosure: (a) the effective relative permittivity; (b) the effective dielectric loss tangent.

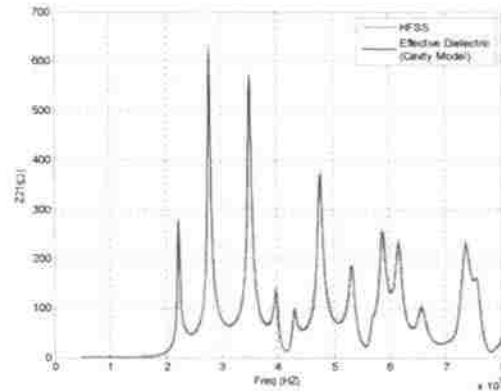


Fig. 11. The transfer impedance calculated using the effective dielectric property and the result by a full-wave simulation tool.

#### IV. CONCLUSION

The paper proposed an effective dielectric property for layered media for the cavity model application. The equation for effective complex permittivity is derived and solved numerically. When the thickness of each layer is much smaller than the wavelength of the highest frequency, the effective complex permittivity has an approximate analytical formula. This paper discusses two- and three-layer cases only, but the approach can be generalized to any number of dielectric layers. The effective dielectric property is validated using both full-wave simulations and measurements. The analytical solution for effective dielectric property is suitable for calculating noise coupling inside PCBs since then assumption of a thin dielectric layer holds. In the case of a metallic enclosure with layered media, the thickness of each dielectric layer may not be smaller than the wavelength, and the effective permittivity can be found only numerically. The effective dielectric property makes the cavity model applicable to layered media, especially in the applications of PCBs and metallic enclosures.



## V. REFERENCE

- [1] R. R. Tummala, E. J. Rymaszewski and A. G. Klopfenstein, *Microelectronics Packaging Handbook, Part I, Ch. 3, Second Ed.*, Chapman & Hall, 1997.
- [2] R. Sorrentino, "Planar circuits, waveguide models, and segmentation method," *IEEE Trans. Microw. Theory Tech.*, vol. MTT-33, pp. 1057–1066, Oct. 1985.
- [3] T. Okoshi, *Planar Circuits for Microwaves and Lightwaves*. Berlin, Germany: Springer-Verlag, 1985, pp. 10–42.
- [4] N. Na, J. Choi, S. Chun, M. Swaminatham, and J. Srinivasan, "Modeling and transient Simulation of planes in electronic packages," *IEEE Transaction on Advanced Packaging*, Vol. 23, No. 3, Aug. 2000, pp. 340–352.
- [5] G. T. Lei, R. W. Techentin, P. R. Hayes, D. J. Schwab, and B. K. Gilbert, "Wave model solution to the ground/power plane noise problem," *IEEE Trans. Instrum. Meas.*, vol. 44, no. 2, pp. 300–303, Apr. 1995.
- [6] G. T. Lei, R. W. Techentin, and B. K. Gilbert, "High-frequency characterization of power/ground-plane structures," *IEEE Trans. Microwave Theory Tech.*, vol. 47, pp. 562–569, May 1999.
- [7] C. Wang, J. Mao, G. Selli, S. Luan, L. Zhang, J. Fan, D. J. Pommerenke, R. E. DuBroff, and J. L. Drewniak, "An efficient approach for power delivery network design with closed-form expressions for parasitic interconnect inductances," *IEEE Trans. Adv. Packag.*, vol. 29, pp. 320-334, 2006.
- [8] T. Okoshi, *Planar Circuits for Microwaves and Lightwaves*. Berlin, Germany: Springer-Verlag, 1985, pp 87–96.

- [9] T. Okoshi, Y. Uehara, and T. Takeuchi, "The segmentation method—an approach to the analysis of microwave planar circuits," *IEEE Trans. Microw. Theory Tech.*, vol. MTT-24, pp. 662-668, Oct. 1976.
- [10] R. Chadha, and K. C. Gupta, "Segmentation method using impedance matrices for analysis of planar microwave circuits," *IEEE Trans. Microw. Theory Tech.*, vol. MTT-29, pp. 71-74, 1981.
- [11] Gang Feng, Selli, G., Chand, K., Mauro Lai, Liang Xue, Drewniak, J.L., Archambeault, B., Connor, S., "Analysis of noise coupling result from overlapping power areas within power delivery networks," 2006 IEEE International Symposium on Electromagnetic Compatibility, vol. 2, pp. 304 – 309, August 2006.
- [12] Yaojiang Zhang, Xiaopeng Dong, Zhenwei Yu, Francesco de Paulis, Gang Feng, Jason A. Mix, Daniel Hua, Kevin Slattery, and Jun Fan, "Efficient Prediction of RF Interference in a Shielding Enclosure with PCBs Using a General Segmentation Method." in EMC Europe 2008, Hamburg, Germany, September 8-12.
- [13] H. Hasegawa, M. Furukawa and H. Yanai, "Properties of Microstrip Line on Si-SiO<sub>2</sub> System," *IEEE Trans. Microw. Theory Tech.*, vol. MTT-19, Nov. 1971, pp 869-881.

## IV. Multimode S-Parameter Characterization for Multiport Passive Structures

Zhenwei Yu, Student Member, IEEE, and Jun Fan, Senior Member, IEEE

*Abstract*—This work develops a unified s-parameter (multimode s-parameter) representation for multiport passive structures. Both mixed-mode and single-ended s-parameters are included in the unified representation, which makes it more convenient to characterize structures including both differential and single-ended ports like printed circuit boards with multiple traces and vias. The transformation between the new multimode and single-ended s-parameter is derived. The multi-mode s-parameter can be implemented into a simulation tool, and has many applications in noise-coupling and EMI problem studies.

### I. INTRODUCTION

A lot of research has been focused on combining single-ended s-parameter and mixed mode s-parameter [1]-[6]. The word multi-mode means the s-matrix includes both single-ended and mixed-mode s-parameter. Assume a mixed-mode port M comprises two single-ended ports P<sub>1</sub> and P<sub>2</sub>, namely

$$\begin{cases} V_d = V_1 - V_2 \\ I_d = \frac{1}{2}(I_1 - I_2) \\ V_c = \frac{1}{2}(V_1 + V_2) \\ I_c = (I_1 + I_2) \end{cases} \quad (1)$$

where  $V_d$  and  $I_d$  are the differential-mode voltage and current between port P<sub>1</sub> and P<sub>2</sub>;  $V_c$  and  $I_c$  are common-mode voltage and current between port P<sub>1</sub> and P<sub>2</sub>;  $V_1$ ,  $V_2$ ,  $I_1$ , and  $I_2$  are voltages and currents at single-ended ports. Equation (1) can be formulated as

$$\sqrt{Z_d}(a_d + b_d) = \sqrt{Z_0}(a_1 + b_1) - \sqrt{Z_0}(a_2 + b_2) \quad (2)$$

where  $Z_d$  is the characteristic impedance of differential mode at the transmission line:

the symbols  $a_d$  and  $b_d$  are the incident and reflective power waves of differential mode;

the symbol  $Z_0$  is the characteristic impedance of the single-ended reference transmission

line; the symbols  $a_1$  and  $b_1$  are the incident and reflective power waves at the single-

ended reference transmission line; the symbols  $a_2$  and  $b_2$  are the incident and reflective

power waves at the single-ended reference transmission line. Since the reference

transmission lines for mixed-mode are assumed to be uncoupled, namely

$$\begin{cases} Z_d = 2Z_0 \\ Z_c = \frac{1}{2}Z_0 \end{cases} \quad (3)$$

Substitute (3) into (2) and it becomes

$$(a_d + b_d) = \frac{1}{\sqrt{2}}(a_1 + b_1) - \frac{1}{\sqrt{2}}(a_2 + b_2). \quad (4)$$

Similar equations can be derived from (1), and can be written as

$$\begin{cases} (a_d + b_d) = \frac{1}{\sqrt{2}}(a_1 + b_1) - \frac{1}{\sqrt{2}}(a_2 + b_2) \\ (a_d - b_d) = \frac{1}{\sqrt{2}}(a_1 - b_1) - \frac{1}{\sqrt{2}}(a_2 - b_2) \\ (a_c + b_c) = \frac{1}{\sqrt{2}}(a_1 + b_1) + \frac{1}{\sqrt{2}}(a_2 + b_2) \\ (a_c - b_c) = \frac{1}{\sqrt{2}}(a_1 - b_1) + \frac{1}{\sqrt{2}}(a_2 - b_2) \end{cases} \quad (5)$$

Equation (5) can be written as

$$\begin{cases} a_d = \frac{1}{\sqrt{2}}(a_1 - a_2) \\ b_d = \frac{1}{\sqrt{2}}(b_1 - b_2) \\ a_c = \frac{1}{\sqrt{2}}(a_1 + a_2) \\ b_c = \frac{1}{\sqrt{2}}(b_1 + b_2) \end{cases} \quad (6)$$

More general expression for conversion from single-ended s-parameter to mixed-mode s-parameter can be derived. Assume an  $N$ -port network structure; its single-ended s-parameter matrix is denoted  $S_{N \times N}$ , which satisfies

$$\begin{pmatrix} b_1 \\ \vdots \\ b_n \\ \vdots \\ b_N \end{pmatrix} = S_{N \times N} \begin{pmatrix} a_1 \\ \vdots \\ a_n \\ \vdots \\ a_N \end{pmatrix} \quad (7)$$

where  $b_1, \dots, b_N$  are reflective power wave from Port 1 to Port  $N$ , and  $a_1, \dots, a_N$  are incident power wave from Port 1 to Port  $N$ . Table describes the index mapping from single-ended ports to multi-mode ports. The first row contains multi-mode ports after mode transformation.  $M_1 \dots M_L$  are  $L$  mixed-mode ports, and  $M_{2L+1} \dots M_N$  are  $N-2L$  single-ended ports. Notice  $M_{L+1} \dots M_{2L}$  doesn't exist. The second and third rows contain  $N$  single-ended ports before mode transformation. The port mapping can be found from each column. e.

g., mixed-mode port  $M_l$  ( $1 \leq l \leq L$ ) comprises two single-ended ports  $P_{i(l)}, P_{j(l)}$ .

Subscript  $i(l)$  refers to the index of positive single-ended port before mode transformation and subscript  $j(l)$  refers to the index of negative single-ended port.

Single-ended port  $M_n$  ( $2L+1 \leq n \leq N$ ) are mapped from single-ended port  $P_{k(n)}$ .

Subscript  $k(n)$  refers to the index of the single-ended port before mode transformation.

Table I. The port mapping from single-ended port to mixed-mode port.

$M_1$	...	$M_l$	...	$M_L$	$M_{2L+1}$	...	$M_n$	...	$M_N$
$P_{i(1)}$	...	$P_{i(l)}$	...	$P_{i(L)}$	$P_{k(2L+1)}$	...	$P_{k(n)}$	...	$P_{k(N)}$
$P_{j(1)}$	...	$P_{j(l)}$	...	$P_{j(L)}$					

According to the port index mapping table, one can fill in the N-by-N mode transformation matrix  $Q$  by the following rules: for  $1 \leq l \leq L$ ,

$$\begin{cases} Q(l, i(l)) = \frac{1}{\sqrt{2}} \\ Q(l, j(l)) = -\frac{1}{\sqrt{2}} \\ Q(L+l, i(l)) = \frac{1}{\sqrt{2}} \\ Q(L+l, j(l)) = \frac{1}{\sqrt{2}} \end{cases} \quad (8)$$

for  $2L+1 \leq n \leq N$ ,

$$Q(n, k(n)) = 1; \quad (9)$$

the rest elements of  $Q$  matrix are all zeros.

The multi-mode s-parameter matrix  $S_{multi}$  can be obtained by

$$S_{multi} = QS_{N \times N}Q^{-1}, \quad (10)$$

and it satisfies

$$\begin{bmatrix} b_{d1} \\ \vdots \\ b_{dl} \\ b_{c1} \\ \vdots \\ b_{cl} \\ b_{2l+1} \\ \vdots \\ b_N \end{bmatrix} = S_{multi} \begin{bmatrix} a_{d1} \\ \vdots \\ a_{dl} \\ a_{c1} \\ \vdots \\ a_{cl} \\ a_{2l+1} \\ \vdots \\ a_N \end{bmatrix}. \quad (11)$$

Furthermore,  $S_{multi}$  can be described by

$$S_{multi} = \begin{bmatrix} S_{dd} & S_{dc} & S_{ds} \\ S_{cd} & S_{cc} & S_{cs} \\ S_{sd} & S_{sc} & S_{ss} \end{bmatrix}. \quad (12)$$

$S_{dd}$  is called differential  $s$ -parameters;  $S_{cc}$  is called common-mode  $s$ -parameters;  $S_{ds}$  and  $S_{cd}$  are called mode-conversion  $s$ -parameters [1].  $S_{ds}$  describes the conversion of differential-mode waves to waves at single-ended ports;  $S_{cs}$  describes the conversion of common-mode waves to waves at single-ended ports;  $S_{sd}$  describes the conversion of waves at single-ended ports to differential mode waves;  $S_{sc}$  describes the conversion of waves at single-ended ports to common-mode waves; and  $S_{ss}$  are the single-ended  $s$  parameters.

## II. EXAMPLES

Two examples are given to demonstrate the proposed mode conversion approach from single-ended port to the mixed-mode Example 1 is a 4-layer printed circuit board (PCB) with multiple vias. Five single-ended ports  $P_1, \dots, P_5$  are defined between vias and nearby planes as labeled in the figure, and the following relationship holds:

$$\begin{bmatrix} b_1 \\ b_2 \\ b_3 \\ b_4 \\ b_5 \end{bmatrix} = S_{5 \times 5} \begin{bmatrix} a_1 \\ a_2 \\ a_3 \\ a_4 \\ a_5 \end{bmatrix} \quad (13)$$

where  $a_i$  and  $b_i$  are incident and reflective wave at singled port  $P_i$ .

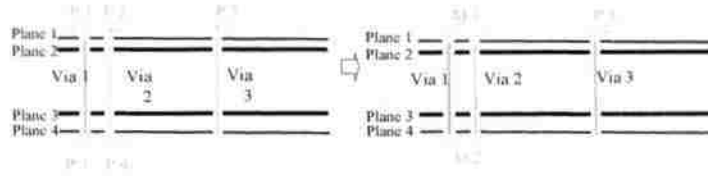


Fig. 1. A 4-layer printed circuit board with multiple vias.

$M_1$  is a mixed-mode port comprising single-ended ports  $P_1$  and  $P_2$ , and  $M_2$  is a mixed-mode port comprising single-ended ports  $P_3$  and  $P_4$ . For mixed-mode ports  $M_1$ ,  $M_2$  and single-ended port  $P_5$ , the multi-mode  $s$ -parameter matrix can be constructed by (9), and the transform matrix  $Q$  can be filled in by (7) and (8), and it becomes

$$Q = \begin{bmatrix} \frac{1}{\sqrt{2}} & -\frac{1}{\sqrt{2}} & 0 & 0 & 0 \\ 0 & 0 & \frac{1}{\sqrt{2}} & -\frac{1}{\sqrt{2}} & 0 \\ \frac{1}{\sqrt{2}} & \frac{1}{\sqrt{2}} & 0 & 0 & 0 \\ 0 & 0 & \frac{1}{\sqrt{2}} & \frac{1}{\sqrt{2}} & 0 \\ 0 & 0 & 0 & 0 & 1 \end{bmatrix}. \quad (14)$$

$S_{multi}$  satisfies



$$\begin{pmatrix} b_{d1} \\ b_{d2} \\ b_{c1} \\ b_{c2} \\ b_5 \end{pmatrix} = S_{multi} \begin{pmatrix} a_{d1} \\ a_{d2} \\ a_{c1} \\ a_{c2} \\ a_5 \end{pmatrix} \quad (15)$$

where  $a_{di}$  and  $b_{di}$  are differential-mode incident and reflective wave at port  $M_i$ , and  $a_{ci}$  and  $b_{ci}$  are common-mode incident and reflective wave at port  $M_i$ .

Another example is a set of dipole and monopole antennas, as shown in Fig. 2. Two folded dipoles and three monopoles are included; for each folded dipole, e. g., the first folded dipole on the left, two single-ended ports  $P_1$  and  $P_2$  are defined between the ends of the dipole and the ground plane; for each monopole, one single-ended port is defined at the end of the monopole and the ground plane. The symbols  $P_1, P_2, \dots, P_7$  are single-ended ports, which satisfies

$$\begin{bmatrix} b_1 \\ b_2 \\ b_3 \\ b_4 \\ b_5 \\ b_6 \\ b_7 \end{bmatrix} = S_{7,7} \begin{bmatrix} a_1 \\ a_2 \\ a_3 \\ a_4 \\ a_5 \\ a_6 \\ a_7 \end{bmatrix} \quad (16)$$

where  $b_i$  ( $i=1,2,\dots,7$ ) represents reflected wave from the port  $P_i$ , and  $a_i$  represents the reflected incident wave from the port  $P_i$ . The symbols  $M_1, M_2, M_5, M_6$ , and  $M_7$  denote multimode ports:  $M_1$  is the mixed-mode port comprising the single-ended ports  $P_1$  and  $P_2$ ;  $M_2$  is the mixed-mode port comprising the single-ended ports  $P_3$  and  $P_4$ ;  $M_5, M_6$ , and  $M_7$  are single ended ports. The multimode s-parameter  $S_{multi}$  satisfies

$$\begin{pmatrix} b_{d1} \\ b_{d2} \\ b_{c1} \\ b_{c2} \\ b_5 \\ b_6 \\ b_7 \end{pmatrix} = S_{multi} \begin{pmatrix} a_{d1} \\ a_{d2} \\ a_{c1} \\ a_{c2} \\ a_5 \\ a_6 \\ a_7 \end{pmatrix} \quad (17)$$

where  $a_{di}$  and  $b_{di}$  ( $i=1,2$ .) are differential-mode incident and reflective wave at port  $M_i$ ;  $a_{ci}$  and  $b_{ci}$  ( $i=1,2$ .) are common-mode incident and reflective wave at port  $M_i$ ;  $a_i$  and  $b_i$  ( $i=5, 6, \text{ and } 7$ .) are the incident and reflective wave at port  $P_5, P_6$  and  $P_7$ . According to the matrix filling steps described in (8) and (9), the transform matrix  $Q$  from  $S_{7 \times 7}$  to  $S_{multi}$  can be written as:

$$Q = \begin{bmatrix} \frac{1}{\sqrt{2}} & -\frac{1}{\sqrt{2}} & 0 & 0 & 0 & 0 & 0 \\ 0 & 0 & \frac{1}{\sqrt{2}} & -\frac{1}{\sqrt{2}} & 0 & 0 & 0 \\ \frac{1}{\sqrt{2}} & \frac{1}{\sqrt{2}} & 0 & 0 & 0 & 0 & 0 \\ 0 & 0 & \frac{1}{\sqrt{2}} & \frac{1}{\sqrt{2}} & 0 & 0 & 0 \\ 0 & 0 & 0 & 0 & 1 & 0 & 0 \\ 0 & 0 & 0 & 0 & 0 & 1 & 0 \\ 0 & 0 & 0 & 0 & 0 & 0 & 1 \end{bmatrix}. \quad (18)$$

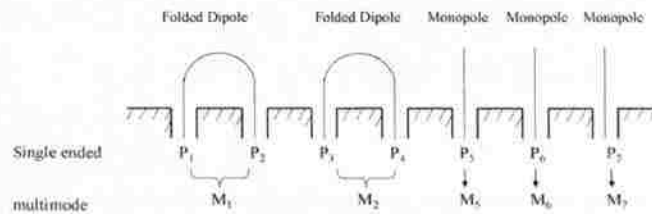


Fig. 2. A set of dipole and monopole antennas.

The physical meaning of each element in  $S_{multi}$  can be also explained. If a differential mode incident wave  $a_{d1}$  comes towards the mixed-mode port  $M_1$ , and all other ports are well matched, then the reflected wave from the single-ended port  $P_5$  is  $b_5 = a_{d1}S_{multi}(5,1)$ . If a differential mode incident wave comes into mixed-mode port  $M_2$  is  $a_{d2}$ , and all other ports are well matched, then the common mode reflected wave from mixed-mode port  $M_1$  is  $b_{c1} = a_{d2}S_{multi}(3,2)$ . If an incident wave comes into single-ended port 6 is  $a_6$ , and all other ports are well matched, then the common mode reflected wave from mixed-mode port  $M_2$  is  $b_{c2} = a_6S_{multi}(4,6)$ .

### III. CONCLUSIONS

A unified  $s$ -parameter (multimode  $s$ -parameter) representation for multiport passive structures is proposed in this work. With both single-ended and mixed-mode  $s$ -parameters in one  $s$ -matrix, it becomes more straightforward to characterize structures including both differential and single-ended ports, e. g., a printed circuit board with multiple traces and vias. The transformation from a single-ended  $s$ -matrix to the multimode  $s$ -matrix is derived. The physical meaning of the proposed multimode  $s$ -parameter representation is discussed, and this representation has many applications in noise-coupling and EMI problem studies.

### IV. REFERENCES

- [1] A. Ferrero and M. Pirola, "Generalized Mixed-Mode S-Parameters," *IEEE Trans. Microwave Theory Tech.*, vol. 54, pp. 458-463, 2006.

- [2] D. E. Bockelman, W. R. Eisenstadt, "Combined Differential and Common-Mode Scattering Parameters: Theory and Simulation," *IEEE Trans. Microwave Theory Tech.*, vol. 43, pp. 1530-1539, 1995.
- [3] D. E. Bockelman and W. R. Eisenstadt, "Pure-mode network analyzer for on-wafer measurements of mixed-mode  $S$ -parameters of differential circuits," *IEEE Trans. Microwave Theory Tech.*, vol. 45, no. 7, pp.1071-1077, Jul. 1997.
- [4] D. E. Bockelman, W. R. Eisenstadt and R. Stengel, "Accuracy estimation of mixed-mode scattering parameter measurements," *IEEE Trans. Microwave Theory and Tech.*, vol. 47, no. 1, pp. 102-105, 1999.
- [5] K. Kurokawa, "Power Waves and the Scattering Matrix," *IEEE Trans. Microwave Theory and Tech.*, vol. 13, no. 2, pp. 194-202, 1965.
- [6] W. Fan, A. Lu, L. L. Wai and B. K. Lok, "Mixed-mode  $S$ -parameter characterization of differential structures," in *Electronics Packaging Technology, 2003 5th Conference*, pp. 533-537, Dec. 2003.

## 2. CONCLUSIONS

Faced with the growing market of wireless devices such as smartphones, laptop computers, wireless platforms require tighter integration and run at higher frequencies. An effective RFI model can help wireless platform producers deliver differentiated products with excellent RFI/EMI performance at lower costs. Noise characterization from IC radiated emissions is one of the main areas in the RFI modeling research.

In this dissertation a physical dipole model for IC radiated emissions based on the near field scanning data is proposed. An array of electric dipoles and magnetic dipoles are chosen to model the IC. The dipoles are placed at some distance above the ground plane, and their values are calculated from the near-field data. A trace structure is simulated as an example and equivalent dipoles are extracted based on the “scanned” field data above the trace. The result shows that the values of dipoles are quantitatively relate to the current and voltage distributions in the trace, which demonstrates that the model reflects the physics in a DUT. The fields above the scanning plane is predicted using the dipole model, and agree with the simulated results very well. An example IC structure was also built and near-field scanning was performed to validate this model experimentally. Another advantage of this dipole model is that they are extracted to model the IC only, and do not include the effect of the ground plane. This means the physical dipoles can be placed in an environment with other metallic structures to predict radiated emissions. The dipole model is placed under heat sinks to predict its near- and far-fields, and the results agree with simulation as well. In the RFI study, it is possible to build a library of the physical dipole models for ICs, and the model for each IC can be imported into a full-wave simulation tool to calculate emissions. This would help

designers to predict possible RFI problems caused by an IC, and shorten the period of product development.

In terms of heat-sink radiation emission prediction, an approach is proposed to incorporate the equivalent dipole-moment model of an IC into the heat-sink model as its excitation. By using a more realistic excitation for heat-sink modeling, both the near-field coupling and the far-field radiation from the heat sink can be accurately evaluated. And, thus, meaningful optimizations of heat-sink geometries and noise mitigation designs become possible. The requirements for suitable IC models in this application are discussed, and an improved dipole-moment model based on near-field scanning is presented. The accuracy and the effectiveness of this approach are demonstrated by two simple examples.

An approach to obtain effective dielectric properties for layered media is proposed for the cavity model application. The equation for effective complex permittivity is derived and solved numerically. When the thickness of each layer is much smaller than the wavelength of the highest frequency, the effective complex permittivity has an approximate analytical formula. This paper discusses two- and three-layer cases only, but the approach can be generalized to any number of dielectric layers. The effective dielectric properties are validated using full-wave simulations. The analytical solution for effective dielectric properties is suitable for calculating noise coupling inside PCBs since then the assumption of thin dielectric layers holds. In the case of a metallic enclosure with layered media, the thickness of each dielectric layer may not be smaller than the wavelength, and the effective permittivity can be found only numerically. The effective dielectric properties make the cavity model applicable for layered media.

especially in the applications of PCBs and metallic enclosures. Future works includes experimental validation of effective dielectric properties.

A unified  $s$ -parameter (multimode  $s$ -parameter) representation for multiport passive structures is proposed in this work. With both single-ended and mixed-mode  $s$ -parameters in one  $s$ -matrix, it becomes more straightforward to characterize structures including both differential and single-ended ports, e. g., a printed circuit board with multiple traces and vias. The transformation from a single-ended  $s$ -matrix to the multimode  $s$ -matrix is derived. The physical meaning of the proposed multimode  $s$ -parameter representation is discussed, and this representation has many applications in noise-coupling and EMI problem studies.

Another direction on the IC radiated emission is statistical source modeling. In the current source modeling approach, while considering radiated emissions in the frequency domain, the source is synthesized and the phase reference is given by the source. However, when the emissions are random, there is no phase reference defined, which makes traditional NF techniques impractical. A statistical model is more desirable than a deterministic model to describe the IC radiation. Future work includes a statistical model for IC radiated emissions based on near-field scanning.

## VITA

Zhenwei Yu was born in Huangshi, Hubei Province, P. R. China. He received the Bachelor of Science degree in Maths and Physics (2005) and the Master of Engineering degree in Electrical Engineering (2007) from Tsinghua University, Beijing, P. R. China. He was a Co-op at IBM, Research Triangle Park, NC, in 2009, and was a Co-op at Intel Labs, Hillsboro, OR, in 2011. His research interests include signal integrity, radio frequency interference mitigation, and electromagnetic interference mitigation. In May, 2012, he received his Ph. D. in Electrical Engineering from Missouri University of Science and Technology.